Causes of ice age intensification across the Mid-Pleistocene Transition

Thomas B. Chalk[a,b,1,2], Mathis P. Hain[a,1,2], Gavin L. Foster[a], Eelco J. Rohling[a,c], Philip F. Sexton[d], Marcus P. S. Badger[d,e], Soraya G. Cherry[a], Adam P. Hasenfratz[f], Gerald H. Haug[g], Samuel L. Jaccard[h,i], Alfredo Martínez-García[g], Heiko Pälike[a,j], Richard D. Pancost[e], and Paul A. Wilson[a]

[a]Ocean and Earth Science, University of Southampton, National Oceanography Centre Southampton, Southampton SO14 3ZH, United Kingdom; [b]Department of Physical Oceanography, Woods Hole Oceanographic Institution, Woods Hole, MA 02543; [c]Research School of Earth Sciences, The Australian National University, Canberra 2601, Australia; [d]School of Environment, Earth and Ecosystem Sciences, The Open University, Milton Keynes MK7 6AA, United Kingdom; [e]Organic Geochemistry Unit, School of Chemistry, The Cabot Institute, University of Bristol, Bristol BS8 1TS, United Kingdom; [f]Geologisches Institut, Eidgenössische Technische Hochschule Zürich, 8092 Zürich, Switzerland; [g]Max Planck Institut für Chemie, 55128 Mainz, Germany; [h]Institute of Geological Sciences, University of Bern, 3012 Bern, Switzerland; [i]Oeschger Center for Climate Change Research, University of Bern, 3012 Bern, Switzerland; and [j]Center for Marine Environmental Sciences (MARUM), University of Bremen, 28359 Bremen, Germany

Edited by Maureen E. Raymo, Lamont–Doherty Earth Observatory of Columbia University, Palisades, NY, and approved September 7, 2017 (received for review February 9, 2017)

During the Mid-Pleistocene Transition (MPT; 1,200–800 kya), Earth's orbitally paced ice age cycles intensified, lengthened from ∼40,000 (∼40 ky) to ∼100 ky, and became distinctly asymmetrical. Testing hypotheses that implicate changing atmospheric CO_2 levels as a driver of the MPT has proven difficult with available observations. Here, we use orbitally resolved, boron isotope CO_2 data to show that the glacial to interglacial CO_2 difference increased from ∼43 to ∼75 μatm across the MPT, mainly because of lower glacial CO_2 levels. Through carbon cycle modeling, we attribute this decline primarily to the initiation of substantive dust-borne iron fertilization of the Southern Ocean during peak glacial stages. We also observe a twofold steepening of the relationship between sea level and CO_2-related climate forcing that is suggestive of a change in the dynamics that govern ice sheet stability, such as that expected from the removal of subglacial regolith or interhemispheric ice sheet phase-locking. We argue that neither ice sheet dynamics nor CO_2 change in isolation can explain the MPT. Instead, we infer that the MPT was initiated by a change in ice sheet dynamics and that longer and deeper post-MPT ice ages were sustained by carbon cycle feedbacks related to dust fertilization of the Southern Ocean as a consequence of larger ice sheets.

boron isotopes | MPT | geochemistry | carbon dioxide | paleoclimate

The Mid-Pleistocene Transition (MPT) marks a major shift in the response of Earth's climate system to orbital forcing. During the Early Pleistocene, glacial–interglacial (G-IG) climate cycles were paced by ∼40,000 y (40 ky) obliquity cycles, whereas G-IG cycles after the MPT gradually intensified over multiple obliquity cycles (i.e., 80- to 120-ky periodicity) (1, 2) and acquired a distinctively asymmetric character with gradual glacial growth and abrupt glacial terminations that were paced by a combination of obliquity and precession (1). These changes gave rise to longer, colder, and dustier Late Pleistocene ice ages with larger continental ice sheets and lower global sea level (SL) (3–5) (Fig. 1). The MPT occurred in the absence of any significant change in the pacing or amplitude of orbital forcing, indicating that it arose from an internal change in the response of the climate system rather than a change in external forcing (1, 6, 7).

Proposed explanations for the MPT fall into two primary groups: those that invoke a change in ice sheet dynamics and those that call on some subtle change in the climate system's global energy budget. Two prominent hypotheses posit that either removal of the subglacial regolith beginning at about 1,200 ky (8, 9) or phase-locking of Northern and Southern Hemisphere ice sheets at about 1,000 ky (10) gave rise to deeper and ultimately longer G-IG climate cycles by allowing for a greater buildup of ice independent of a change in CO_2 radiative climate forcing (scenario 1 in Fig. 2). Alternatively, it has been argued that an underlying change in the global carbon cycle could have triggered the MPT through a decline in ΔR_{CO2} [i.e., the radiative climate forcing exerted by CO_2 decline (11–13) (scenario 2 in Fig. 2)]. The continuous 800-ky-long ice core record of atmospheric CO_2 (i.e., compiled by ref. 14) is well-correlated to and shares spectral power with orbital-scale changes in temperature, ice volume, SL, and the oxygen isotopic composition of benthic foraminifera (Figs. 1 and 3). State of the art coupled climate–ice sheet models can simulate climate cycles that are longer than single obliquity cycles, provided that mean CO_2 concentrations are within certain model-dependent bounds (15, 16) (e.g., 200–260 μatm). These studies suggest that the absolute CO_2 level attained during rising obliquity (i.e., during increasing high-latitude Northern Hemisphere summer insolation) may be a critical control that determines whether ice sheets are strictly locked to the ∼40-ky beat of obliquity or survive for longer periods. Recent work has provided some evidence for an overall CO_2 decline since the MPT (11, 17), supporting this view. The study by Hönisch et al. (11), in particular, provides

Significance

Conflicting sets of hypotheses highlight either the role of ice sheets or atmospheric carbon dioxide (CO_2) in causing the increase in duration and severity of ice age cycles ∼1 Mya during the Mid-Pleistocene Transition (MPT). We document early MPT CO_2 cycles that were smaller than during recent ice age cycles. Using model simulations, we attribute this to post-MPT increase in glacial-stage dustiness and its effect on Southern Ocean productivity. Detailed analysis reveals the importance of CO_2 climate forcing as a powerful positive feedback that magnified MPT climate change originally triggered by a change in ice sheet dynamics. These findings offer insights into the close coupling of climate, oceans, and ice sheets within the Earth System.

Author contributions: T.B.C., M.P.H., G.L.F., E.J.R., A.P.H., G.H.H., S.L.J., A.M.-G., R.D.P., and P.A.W. designed research; T.B.C., M.P.H., M.P.S.B., and S.G.C. performed research; T.B.C., M.P.H., G.L.F., E.J.R., P.F.S., S.G.C., H.P., and P.A.W. analyzed data; and T.B.C. and M.P.H. wrote the paper.

The authors declare no conflict of interest.

This article is a PNAS Direct Submission.

Data deposition: The data reported in this paper have been deposited in the Pangaea database (https://doi.pangaea.de/10.1594/PANGAEA.882551).

[1]T.B.C. and M.P.H. contributed equally to this work.

[2]To whom correspondence may be addressed. Email: T.chalk@noc.soton.ac.uk or M.P.Hain@soton.ac.uk.

This article contains supporting information online at www.pnas.org/lookup/suppl/doi:10.1073/pnas.1702143114/-/DCSupplemental.

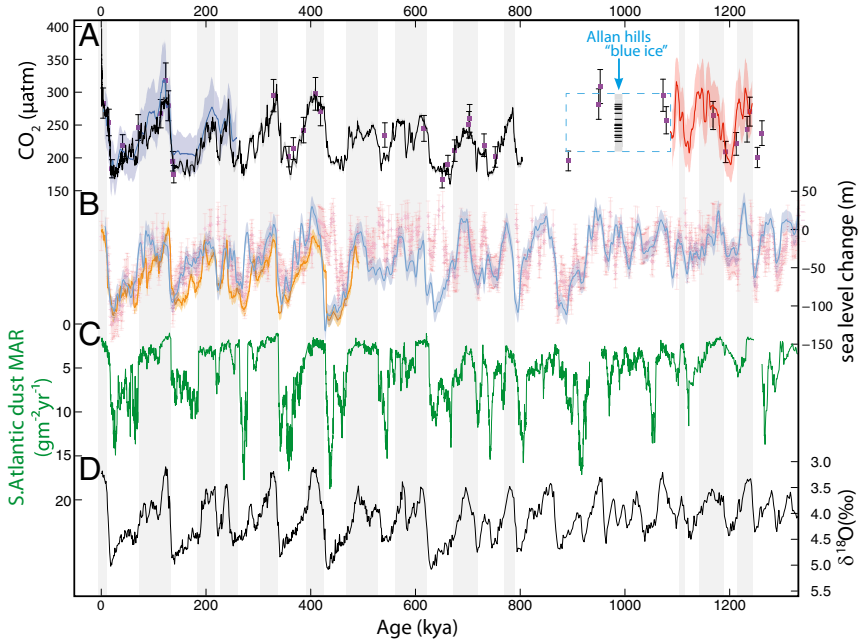

Fig. 1. Climate records across the MPT. (*A*) CO_2 records are shown as follows: black line, ice core compilation (14); blue, our $\delta^{11}B$-based LP260 data; red, our $\delta^{11}B$-based eMPT data; and purple squares, low-resolution MPT $\delta^{11}B$ record of ref. 11 (all with 2σ error bars/envelopes). The range of ice core CO_2 measurements (17) from stratigraphically disturbed blue ice and their approximate ages are indicated. (*B*) SL records, where orange indicates the Red Sea record (21), dark blue represents Mg/Ca-based deconvolution of deep sea benthic foraminiferal oxygen isotope data (3), and pink shows a record from the Mediterranean Sea (4). (*C*) Dust mass accumulation rate (MAR) in a sub-Antarctic site ODP 1090 on the southern flank of the Agulhas Ridge (24). (*D*) LR04 benthic foraminiferal oxygen isotope stack (26). Warm intervals are highlighted by gray bars.

evidence that CO_2 decline was most pronounced during glacial stages. Here, we build on that work with the aim to resolve the coupling of CO_2 and climate on orbital timescales to address major unanswered questions regarding the role of CO_2 change in the MPT.

To better quantify the role of CO_2 during the MPT, we present two orbitally resolved, boron isotope-based CO_2 records generated using the calcite tests of surface-dwelling planktonic foraminifera from Ocean Drilling Program (ODP) Site 999 in the Caribbean (Fig. 3 and Figs. S1 and S2). Boron isotopes ($\delta^{11}B$) in foraminifera have proven to be a reliable indicator of past ocean pH (18, 19) and with appropriate assumptions regarding a second carbonate system parameter (*Materials and Methods* and Fig. S3), allow reconstruction of atmospheric CO_2 levels. Site 999 likely remained near air–sea CO_2 equilibrium through time (20), and this is further supported by agreement of our data (blue and red in Figs. 1*A* and 3) with published low-resolution $\delta^{11}B$-derived CO_2 data from ODP Site 668 in the equatorial Atlantic (11) (purple squares in Figs. 1*A* and 3*B*) and with the ice core CO_2 compilation (14).

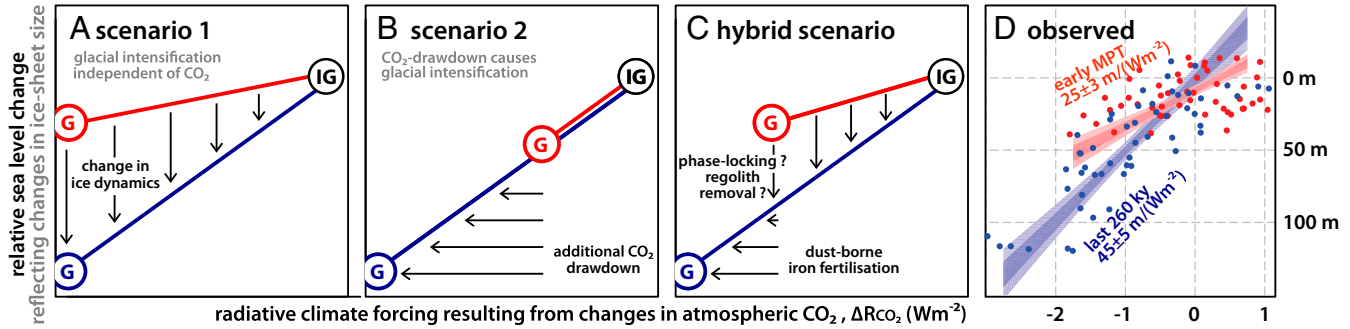

Fig. 2. Changing relationship between CO_2 climate forcing and ice sheet size. Three scenarios (*A*–*C*) for the MPT intensification of glacial cycles compared with observations (*D*). Reconstructed SL is taken here to reflect continental ice sheet size in relationship to CO_2 climate forcing (ΔR_{CO2}) calculated (33) from our orbitally resolved CO_2 data. In all panels, red and blue represent conditions during our two sampling intervals before and after the MPT (i.e., eMPT and LP260), respectively. The end member scenarios posit (*A*) a change in ice sheet dynamics, causing ice volume to become more sensitive to unchanged G-IG climate forcing, and (*B*) an unchanged sensitivity of ice sheet size to forcing, with glacial intensification driven by additional CO_2 drawdown. Neither one of these two scenarios adequately describes both observed changes of increased ice sheet sensitivity (greater slope) and additional glacial CO_2 drawdown (more negative climate forcing). Here, we argue for a hybrid scenario with a change in ice sheet dynamics (possibly caused by regolith removal of ref. 8 or ice sheet phase-locking of ref. 10), allowing ice sheets to grow larger and to trigger a positive ice–dust–CO_2 feedback that promotes additional glacial intensification. In *D*, the regression confidence intervals account for uncertainty in both SL and ΔR_{CO2} (*SI Forcing to SL Relationship*), but to avoid clutter, we only display the regression based on the Mediterranean SL reconstruction (4) and the uncertainty on the slope rather than the individual data points. We refer the reader to *SI Forcing to SL Relationship* and Fig. S7 for other SL records and full treatment of data uncertainties.

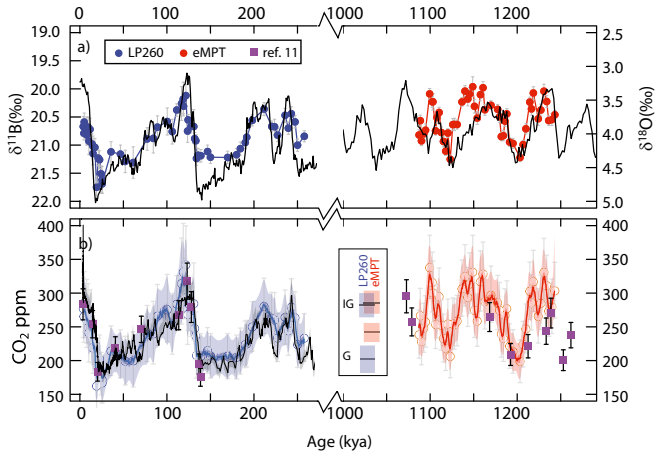

Fig. 3. Reconstructed ice age CO_2 cycles before and after MPT. (*A*) Boron isotope data from ODP 999 (Fig. S1) shown in blue (LP260) and red (eMPT) along with the LR04 deep sea benthic foraminiferal oxygen isotope stack (black) (26). (*B*) CO_2 levels calculated from boron isotopes (same colors as above) compared with ice core (black) (14) and previous low-resolution boron-derived CO_2 data (purple) (11). Probabilistic assessments are shown as the colored bands, with the probability maximum shown within a dark band that represents its 95% probability envelope (~±6 ppm) and a lighter band that represents the full 95% envelope of the sampled distribution. As illustrated by *B*, *Inset*, comparison between our (red) eMPT and (blue) LP260 records reveals that glacials on average experienced higher CO_2 levels during eMPT than LP260 (eMPT: 241 ± 21 µatm vs. LP260: 203 ± 14 µatm; 2σ), whereas interglacial levels were indistinguishable between the two time slices (eMPT: 284 ± 17 µatm vs. LP260: 277 ± 18 µatm; 2σ).

Results

Our two datasets span an early portion of the Mid-Pleistocene Transition (eMPT) from 1,080 to 1,250 kya (n = 51) and for validation against the ice core CO_2 record, the Pleistocene interval from 0 to 260 kya (LP260; n = 59, including 32 recalculated data points from ref. 18), yielding a similar median sampling interval of ~3.5–4.5 ky for both records. Our LP260 CO_2 dataset has a confidence interval of ±20 µatm (2σ) and is offset by a mean of +7 µatm from the ice core CO_2 data when accounting for both CO_2 and age uncertainties (21) (Fig. 3*B* and *SI Methodology*). Comparison between our two CO_2 records reveals that eMPT glacials on average were associated with higher CO_2 levels than LP260 glacials (eMPT: 241 ± 21 µatm vs. LP260: 203 ± 14 µatm; 2σ), whereas interglacial levels were indistinguishable (eMPT: 284 ± 17 µatm vs. LP260: 277 ± 18 µatm; 2σ). This analysis uses highest and lowest 25th percentiles of $\delta^{18}O$ values to define "glacial" and "interglacial" subsets of the data, although this pattern is independent of the thresholds that we define (Fig. 4 and Fig. S4). Our analysis reproduces the glacial stage-specific decline in CO_2 levels found in ref. 11, leading to similar reconstructed increases in the glacial to interglacial CO_2 difference since the MPT (40 ± 47 and 32 ± 35 µatm based on ref. 11 and our data, respectively) (Fig. 4). The higher resolution of these datasets allows this approach to yield useful data about our timespans, despite the relatively large uncertainty on each individual data point. When analyzed in a similar way, recent direct measurements of CO_2 from a stratigraphically disturbed section of ~1-My-old "blue ice" (17) offer a fully independent test for the two $\delta^{11}B$-based reconstructions and are consistent with these findings (Fig. 4 and Fig. S4). Thus, all available evidence suggests that the MPT was associated with a transition in the global carbon cycle characterized mainly by enhanced glacial-stage drawdown of CO_2.

We evaluate the reconstructed G-IG CO_2 change across our study interval with a carbon cycle model inversion of Southern Ocean and Atlantic mechanisms thought to have contributed to the most recent Late Pleistocene G-IG CO_2 cycles (22). For this, we force the CYCLOPS carbon cycle model (23) with ODP 1090 sedimentary iron mass accumulation rates (24), ODP 1094 Ba/Fe ratios (25), and ODP 982/U1313 (Fig. S1) benthic $\Delta\delta^{13}C$ variations (26, 27) to represent, respectively, (*i*) sub-Antarctic dust-borne iron fertilization; (*ii*) combined changes in polar Antarctic stratification, nutrient drawdown, and export production; and (*iii*) transitions in the geometry and depth structure of the Atlantic Meridional Overturning Circulation (AMOC) (Fig. S5). These mechanisms and their model sensitivities have been documented elsewhere (23). Here, we invert the model and the forcing to minimize the mismatch between simulated atmospheric CO_2 levels and the ice core CO_2 record of the last 800 ky (residual rms error of 12.3 µatm) (*SI Carbon Cycle Modeling*) and then, to predict atmospheric CO_2 levels back to 1,500 ky (Fig. S5) for comparison with our data.

We find that changes in the periodicity of simulated CO_2 levels closely match those in the ice core CO_2 record, in the benthic foraminiferal oxygen isotope record, and in our $\delta^{11}B$-based CO_2 reconstruction (Fig. S6). Within the relative age uncertainty between the model forcing and our $\delta^{11}B$ record, we find that the model explains more than 60% of the variance observed in our eMPT CO_2 reconstruction, in line with model and reconstruction uncertainties. The model inversion does not include any secular change in the silicate weathering cycle (11) (*SI Carbon Cycle Modeling*), so that simulated CO_2 change is exclusively related to carbon redistribution within the ocean–atmosphere system and associated $CaCO_3$ compensation dynamics (22, 23).

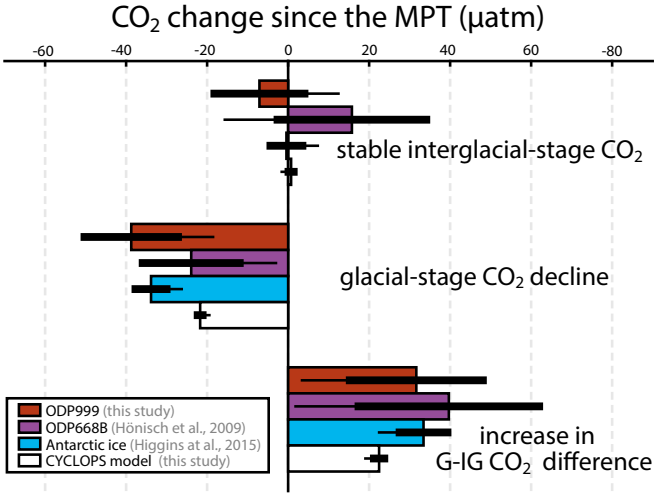

Fig. 4. CO_2 change since the MPT. Quantified from different datasets: boron isotope data from ODP 999 (this study) and ODP 668 (11), CO_2 directly measured on stratigraphically disturbed ~1-My-old blue ice from the Allan Hills (17), and CYCLOPS model inversion (this study). For each dataset, we quantify the change in (*Top*) interglacial and (*Middle*) glacial CO_2 level as well as (*Bottom*) the change in the magnitude of interglacial–glacial CO_2 cycles. For this analysis, we define glacial and interglacial subsets of the datasets based on a 25% cutoff criterion, subsampling the data with the 25% lowest/highest $\delta^{18}O$ (marine records) or CO_2 (ice core; model). As further discussed in *SI Quantification of* $^{G}CO_2$, $^{IG}CO_2$, *and* $^{IG-G}\Delta CO_2$, the results are robust for a wide range of cutoff values (Fig. S4). Thick black bars denote 1σ uncertainty of the estimated CO_2 change, while thin black bars denote the one-sided test of the sign of CO_2 change at 95% significance level. We note that the ODP 668 uncertainties do not encompass the underlying alkalinity and seawater boron isotope composition assumptions, which are included in the uncertainty propagation for our ODP 999 data. The Allan Hills ice may not capture the full range of CO_2 levels (17).

In good agreement with the δ^{11}B-based CO_2 reconstructions and the ice core CO_2 measurements, the model inversion yields (*i*) insignificant (-1 ± 3 μatm; 2σ) eMPT to LP260 interglacial CO_2 change and (*ii*) a -22 ± 5 μatm (2σ) eMPT to LP260 decline in glacial-stage CO_2 levels (Fig. 4 and Fig. S4). In the model, we can attribute most of the additional glacial CO_2 drawdown to MPT intensification of glacial dust-borne iron fertilization of biological productivity and nutrient utilization in the Sub-Antarctic Zone of the Southern Ocean (24, 28–30) (Fig. S5). AMOC shoaling also seems to have become more prevalent after ~1,200 ky but contributes less to simulated CO_2 change (23). The model reproduces relatively low reconstructed interglacial CO_2 from 400 to 800 ky, because use of ODP 1094 Ba/Fe in the model inversion results in persistent polar Southern Ocean stratification as suggested previously (25). Through our eMPT sample interval, the model reproduces the ~80-ky CO_2 periodicity that is evident in our eMPT δ^{11}B data (Fig. S6), mainly because of an ~80-ky periodicity in eMPT polar Antarctic stratification and nutrient cycling recorded in ODP 1094 Ba/Fe (25). While all three forcings (iron fertilization, Atlantic circulation, coupled polar Antarctic changes) contribute to the simulated changes in CO_2 periodicities that are highly coherent with the MPT change in rhythm of the climate system, the iron fertilization influence dominates the MPT intensification of ice age CO_2 drawdown (Fig. S5).

Discussion

MPT intensification of glacial-stage CO_2 drawdown is consistent with stabilization of continental ice sheets during increasing orbital obliquity by reduced greenhouse gas forcing, thereby helping ice sheets to grow larger and for periods longer than one obliquity cycle (scenario 2 in Fig. 2). However, when we directly compare changes in SL as a measure for ice volume against CO_2 climate forcing (ΔR_{CO2}) from our records (Fig. 2*D*), we find that, between eMPT and LP260, ice sheet mass increased progressively more per CO_2 lowering, thereby increasing the SL–ΔR_{CO2} slope in Fig. 2. This suggests an increase in ice sheet sensitivity to CO_2 forcing across the MPT, with the caveat that eMPT may not fully capture pre-MPT conditions, although it agrees with the longer-term record of Hönisch et al. (11). This finding is robust, regardless of which SL reconstruction is used (Fig. S7); in all cases, the SL to ΔR_{CO2} relationships appear to be linear, with increasing slopes from eMPT to LP260. The steepening relationship is also evident when regressing δ^{11}B to δ^{18}O relationships, with both isotope ratios measured on the same sample material (Fig. S8). Using the SL record with the best coverage of both intervals, relative SL from the Mediterranean Sea (4), we estimate 25 ± 3 and 45 ± 5 m of SL lowering for each 1-Wm^{-2} reduction in radiative forcing during eMPT and LP260, respectively. Such a pronounced increase in sensitivity implicates a change in ice sheet dynamics as predicted by the regolith hypothesis (8, 9) or the establishment of marine-based ice sheet margins in East Antarctica (10) (scenario 1 in Fig. 2).

The observed changes in the SL to ΔR_{CO2} relationships contain elements of both end member scenarios shown in Fig. 2 *A* and *B*, in which a greater slope is possibly related to changes internal to the ice sheets (scenario 1) and amplified glacial to interglacial CO_2 climate forcing is linked (this study) to increased glacial dustiness that causes enhanced Southern Ocean iron fertilization (scenario 2). Therefore, we propose a hybrid scenario (Fig. 2*C*) that incorporates both heightened ice sheet sensitivity to CO_2 forcing and dust-driven ocean sequestration of CO_2 to represent the observed climate system change across the MPT.

First, we propose that—independent of orbital and CO_2 forcing—a process internal to the climate system yielded greater glacial buildup of ice sheets [e.g., regolith removal (8) or ice sheet phase-locking (10)]. Second, we infer that larger ice sheets led to increased glacial atmospheric dustiness (31, 32), either directly through SL lowering or indirectly because of atmospheric cooling, drying, and/or changes in surface winds. This, in turn, induced glacial iron fertilization of the Sub-Antarctic Zone of the Southern Ocean, thereby effecting the 20- to 40-μatm increase in the amplitude of the G-IG CO_2 cycles documented here (Fig. 4) (11). In our hybrid scenario, the positive climate–dust–CO_2 feedback is required to (*i*) drive additional ice sheet growth and (*ii*) stabilize those ice sheets during the critical orbital phase of rising obliquity, ensuring the survival of ice sheets beyond single obliquity cycles. Therefore, regardless of the mechanism that served as the initial MPT trigger, our findings further illustrate the exquisite coupling that exists in the Earth System between climate change, ice sheet mass, and the polar ocean mechanisms that regulate G-IG CO_2 change.

Materials and Methods

Globigerinoides ruber white *sensu stricto* (300–355 μm) were picked from sediments from ODP 999A (Fig. S1), and the age model was constructed by benthic oxygen isotopes from the same samples and X-ray fluorescence scanning data. Samples were measured for boron isotope composition using a Thermo Scientific Neptune multicollector inductively coupled plasma mass spectrometer at the University of Southampton according to methods described elsewhere (18). Analytical uncertainty is given by the external reproducibility of repeat analyses of Japanese Geological Survey Porites coral standard at the University of Southampton and is typically <0.2‰ (at 95% confidence). Metal element–calcium ratios (Mg, B, Al) were analyzed using Thermo Element 2XR inductively coupled plasma mass spectrometer at the University of Southampton. Here, these data are used to assess adequacy of clay removal (Al/Ca < 100 μmol/mol) and to generate down core temperature estimates. CO_2 was calculated using a Monte Carlo approach (10,000 replicates) with estimates of salinity and alkalinity using a flat probability spanning a generous range (34–37 psu and 2,100–2,500 μmol/kg, respectively). A normal distribution around proxy data was used for all other input variables (temperature, pH, $\delta^{11}B_{sw}$, $\delta^{11}B_{foram}$) (*SI Methodology* has full details). The CO_2 record was then probabilistically assessed using a Monte Carlo approach that considers uncertainties in both age and CO_2 values and that preserves the stratigraphy of the record, which minimizes age uncertainty in a relative sense between samples (shown as an envelope in Figs. 1 and 3). Each of 2,000 Monte Carlo iterations involved independent random resampling of each sample within its *x* and *y* uncertainty distributions. The stratigraphic constraint prevents age reversals in this resampling procedure. Linear interpolation was performed between resampled points, and the distribution of values thus generated was analyzed per time step for the modal value and its 95% probability interval as well as the 95% probability envelope of data in the sampled distribution (using the 2.5th and 97.5th percentiles). Because uncertainties in both *x* and *y* directions are considered, the record of probability maxima (modes) gives a smoothed representation of the record, with quantified uncertainties (*SI Forcing to SL Relationship*).

Inverse carbon cycle modeling was carried out using the CYCLOPS model (23), with the forward model forcing derived from pertinent paleoceanographic records (25–27) and the forcing scaling parameters inverted to minimize model misfit with respect to the ice core CO_2 record of the last 800 ky. Significant linear correlation with and matching spectral content to our boron isotope-based CO_2 data confirm the skill of the model inversion (Fig. S6). Detailed statistical analysis is carried out to identify and quantify changes in absolute glacial and interglacial CO_2 as well as the G-IG CO_2 range from the model inversion results, our high-resolution CO_2 data, and some previous datasets (11, 17) that are not well dated or lack the required temporal resolution for comparison in the time and/or frequency domains. This analysis is based on estimation of the population means of cumulative probability density of glacial and interglacial subsamples, which were selected based on either available benthic foraminiferal δ^{18}O or CO_2 rank (Fig. 4). Factorial analysis of the validated model allows for the mechanistic attribution to sub-Antarctic iron fertilization of glacial stage-specific CO_2 reduction associated with the MPT interval (Fig. S5, *Bottom*), which is the pattern that we identified as common between model and all three empirical datasets. More detailed descriptions of inverse modeling and model/data cross-validation and statistical quantification of CO_2 change can be found in *SI Carbon Cycle Modeling* and *SI Quantification of* $^{G}CO_2$, $^{IG}CO_2$, *and* $^{IG\text{-}G}\Delta CO_2$, respectively.

ACKNOWLEDGMENTS. We thank J. A. Milton, M. Cooper, A. Michalik, M. Spencer, and members of the "boron-team" at the University of Southampton

for analytical help; the Integrated Ocean Drilling Program (IODP) Gulf Coast core repository for sample provision; and R. James, E. McClymont, R. Greenop, W. Kordesch, J. Higgins, and D. Sigman for discussion. This work used samples provided by the International Ocean Discovery Program, which is sponsored by the US National Science Foundation and participating countries under the management of the Joint Oceanographic Institutions. Research was supported by National Environmental Research Council (NERC) Studentship NE/I528626/1 (to T.B.C.); NERC Grant NE/P011381/1 (to T.B.C., M.P.H., G.L.F., E.J.R., and P.A.W.); NERC Fellowships NE/K00901X/1 (to M.P.H.), NE/I006346/1 (to G.L.F. and R.D.P), and NE/H006273/1 (to R.D.P.); Royal Society Wolfson Awards (to G.L.F. and P.A.W.); Australian Research Council Laureate Fellowship FL1201000050 (to E.J.R.); Swiss National Science Foundation Grant PP00P2-144811 (to S.L.J.); ETH Research Grant ETH-04 11-1 (to S.L.J.); European Research Council Consolidator Grant (ERC CoG) Grant 617462 (to H.P.); and NERC UK IODP Grant NE/F00141X/1 (to P.A.W.).

1. Huybers P (2011) Combined obliquity and precession pacing of late Pleistocene deglaciations. *Nature* 480:229–232.
2. Clark PU, et al. (2006) The middle Pleistocene transition: Characteristics, mechanisms, and implications for long-term changes in atmospheric pCO_2. *Quat Sci Rev* 25: 3150–3184.
3. Elderfield H, et al. (2012) Evolution of ocean temperature and ice volume through the mid-Pleistocene climate transition. *Science* 337:704–709.
4. Rohling EJ, et al. (2014) Sea-level and deep-sea-temperature variability over the past 5.3 million years. *Nature* 508:477–482.
5. McClymont EL, Sosdian SM, Rosell-Melé A, Rosenthal Y (2013) Pleistocene sea-surface temperature evolution: Early cooling, delayed glacial intensification, and implications for the mid-Pleistocene climate transition. *Earth Sci Rev* 123:173–193.
6. Imbrie J, et al. (1993) On the structure and origin of major glaciation cycles. 2. The 100,000-year cycle. *Paleoceanography* 8:699–735.
7. Pisias NG, Moore T (1981) The evolution of Pleistocene climate: A time series approach. *Earth Planet Sci Lett* 52:450–458.
8. Clark PU, Pollard D (1998) Origin of the middle Pleistocene transition by ice sheet erosion of regolith. *Paleoceanography* 13:1–9.
9. Snyder CW (2016) Evolution of global temperature over the past two million years. *Nature* 538:226–228.
10. Raymo ME, Huybers P (2008) Unlocking the mysteries of the ice ages. *Nature* 451: 284–285.
11. Hönisch B, Hemming NG, Archer D, Siddall M, McManus JF (2009) Atmospheric carbon dioxide concentration across the mid-Pleistocene transition. *Science* 324:1551–1554.
12. Raymo ME, Ruddiman WF, Froelich PN (1988) Influence of late Cenozoic mountain building on ocean geochemical cycles. *Geology* 16:649–653.
13. Berger A, Li X, Loutre M (1999) Modelling northern hemisphere ice volume over the last 3 Ma. *Quat Sci Rev* 18:1–11.
14. Bereiter B, et al. (2015) Revision of the EPICA Dome C CO_2 record from 800 to 600 kyr before present. *Geophys Res Lett* 42:542–549.
15. Abe-Ouchi A, et al. (2013) Insolation-driven 100,000-year glacial cycles and hysteresis of ice-sheet volume. *Nature* 500:190–193.
16. Ganopolski A, Calov R (2011) The role of orbital forcing, carbon dioxide and regolith in 100 kyr glacial cycles. *Clim Past* 7:1415–1425.
17. Higgins JA, et al. (2015) Atmospheric composition 1 million years ago from blue ice in the Allan Hills, Antarctica. *Proc Natl Acad Sci USA* 112:6887–6891.
18. Foster GL (2008) Seawater pH, pCO_2 and CO_3^{2-} variations in the Caribbean Sea over the last 130 kyr: A boron isotope and B/Ca study of planktic foraminifera. *Earth Planet Sci Lett* 271:254–266.
19. Hönisch B, Hemming NG, Loose B (2007) Comment on "A critical evaluation of the boron isotope-pH proxy: The accuracy of ancient ocean pH estimates" by M. Pagani, D. Lemarchand, A. Spivack and J. Gaillardet. *Geochim Cosmochim Acta* 71:1636–1641.
20. Martínez-Botí MA, et al. (2015) Plio-Pleistocene climate sensitivity evaluated using high-resolution CO_2 records. *Nature* 518:49–54.
21. Grant KM, et al. (2014) Sea-level variability over five glacial cycles. *Nat Commun* 5:5076.
22. Sigman DM, Hain MP, Haug GH (2010) The polar ocean and glacial cycles in atmospheric $CO(_2)$ concentration. *Nature* 466:47–55.
23. Hain MP, Sigman DM, Haug GH (2010) Carbon dioxide effects of Antarctic stratification, North Atlantic Intermediate Water formation, and subantarctic nutrient drawdown during the last ice age: Diagnosis and synthesis in a geochemical box model. *Global Biogeochem Cycles* 24:GB4023.
24. Martínez-Garcia A, et al. (2011) Southern Ocean dust-climate coupling over the past four million years. *Nature* 476:312–315.
25. Jaccard SL, et al. (2013) Two modes of change in Southern Ocean productivity over the past million years. *Science* 339:1419–1423.
26. Lisiecki LE, Raymo ME (2005) A Pliocene-Pleistocene stack of 57 globally distributed benthic $\delta^{18}O$ records. *Paleoceanography* 20:PA1003.
27. Lang DC, et al. (2014) The transition on North America from the warm humid Pliocene to the glaciated Quaternary traced by eolian dust deposition at a benchmark North Atlantic Ocean drill site. *Quat Sci Rev* 93:125–141.
28. Ridgwell A (2003) Implications of the glacial CO_2 "iron hypothesis" for Quaternary climate change. *Geochem Geophys Geosyst* 4:1076.
29. Martínez-García A, et al. (2014) Iron fertilization of the Subantarctic ocean during the last ice age. *Science* 343:1347–1350.
30. Martin JH, Gordon RM, Fitzwater SE (1990) Iron in Antarctic waters. *Nature* 345: 156–158.
31. McGee D, Broecker WS, Winckler G (2010) Gustiness: The driver of glacial dustiness? *Quat Sci Rev* 29:2340–2350.
32. Kohfeld KE, Harrison SP (2001) DIRTMAP: The geological record of dust. *Earth Sci Rev* 54:81–114.
33. Myhre G, Highwood EJ, Shine KP, Stordal F (1998) New estimates of radiative forcing due to well mixed greenhouse gases. *Geophys Res Lett* 25:2715–2718.
34. Foster GL, Rae JWB (2016) Reconstructing ocean pH with boron isotopes in foraminifera. *Annu Rev Earth Planet Sci* 44:207–237.
35. Takahashi T, et al. (2009) Climatological mean and decadal change in surface ocean pCO_2, and net sea–air CO_2 flux over the global oceans. *Deep Sea Res Part II Top Stud Oceanogr* 56:554–577.
36. Henehan MJ, et al. (2013) Calibration of the boron isotope proxy in the planktonic foraminifera *Globigerinoides ruber* for use in palaeo-CO_2 reconstruction. *Earth Planet Sci Lett* 364:111–122.
37. Edgar KM, Anagnostou E, Pearson PN, Foster GL (2015) Assessing the impact of diagenesis on $\delta^{11}B$, $\delta^{13}C$, $\delta^{18}O$, Sr/Ca and B/Ca values in fossil planktic foraminiferal calcite. *Geochim Cosmochim Acta* 166:189–209.
38. Paillard D, Labeyrie L, Yiou P (1996) Analyseries 1.0: A Macintosh software for the analysis of geographical time-series. *Eos* 77:379.
39. Schmidt MW, Vautravers MJ, Spero HJ (2006) Western Caribbean sea surface temperatures during the late Quaternary. *Geochem Geophys Geosyst* 7:Q02P10.
40. Barker S, Greaves M, Elderfield H (2003) A study of cleaning procedures used for foraminiferal Mg/Ca paleothermometry. *Geochem Geophys Geosyst*, 10.1029/2003GC000559.
41. Yu JM, Elderfield H (2007) Benthic foraminiferal B/Ca ratios reflect deep water carbonate saturation state. *Earth Planet Sci Lett* 258:73–86.
42. Rae JW, Foster GL, Schmidt DN, Elliott T (2011) Boron isotopes and B/Ca in benthic foraminifera: Proxies for the deep ocean carbonate system. *Earth Planet Sci Lett* 302: 403–413.
43. Foster GL, et al. (2013) Interlaboratory comparison of boron isotope analyses of boric acid, seawater and marine $CaCO_3$ by MC-ICPMS and NTIMS. *Chem Geol* 358:1–14.
44. Evans D, Müller W (2012) Deep time foraminifera Mg/Ca paleothermometry: Nonlinear correction for secular change in seawater Mg/Ca. *Paleoceanography* 27: PA4205.
45. Fantle MS, DePaolo DJ (2006) Sr isotopes and pore fluid chemistry in carbonate sediment of the Ontong Java Plateau: Calcite recrystallization rates and evidence for a rapid rise in seawater Mg over the last 10 million years. *Geochim Cosmochim Acta* 70:3883–3904.
46. Delaney ML, Bé AWH, Boyle EA (1985) Li, Sr, Mg, and Na in foraminiferal calcite shells from laboratory culture, sediment traps, and sediment cores. *Geochim Cosmochim Acta* 49:1327–1341.
47. Klochko K, Kaufman AJ, Yao WS, Byrne RH, Tossell JA (2006) Experimental measurement of boron isotope fractionation in seawater. *Earth Planet Sci Lett* 248:276–285.
48. Catanzaro EJ (1970) *Boric Acid: Isotopic and Assay Standard Reference Materials* (US National Bureau of Standards, Gaithersburg, MD), Special Publication 260-17.
49. Hemming NG, Reeder RJ, Hanson GN (1995) Mineral-fluid partitioning and isotopic fractionation of boron in synthetic calcium carbonate. *Geochim Cosmochim Acta* 59: 371–379.
50. Hemming NG, Hanson GN (1992) Boron isotopic composition and concentration in modern marine carbonates. *Geochim Cosmochim Acta* 56:537–543.
51. Dickson AG (1990) Thermodynamics of the dissociation of boric acid in synthetic seawater from 273.15 to 318.15 K. *Deep Sea Res A Oceanogr Res Pap* 37:755–766.
52. Foster GL, von Strandmann P, Rae JWB (2010) Boron and magnesium isotopic composition of seawater. *Geochem Geophys Geosyst*, 10.1029/2010GC003201.
53. Foster GL, Lear CH, Rae JWB (2012) The evolution of pCO_2, ice volume and climate during the middle Miocene. *Earth Planet Sci Lett* 341–344:243–254.
54. Raitzsch M, Hönisch B (2013) Cenozoic boron isotope variations in benthic foraminifers. *Geology* 41:591–594.
55. Lemarchand D, Gaillardet J, Lewin E, Allegre C (2002) Boron isotope systematics in large rivers: Implications for the marine boron budget and paleo-pH reconstruction over the Cenozoic. *Chem Geol* 190:123–140.
56. Toggweiler J (1999) Variation of atmospheric CO_2 by ventilation of the ocean's deepest water. *Paleoceanography* 14:571–588.
57. Farrell JW, Prell WL (1991) Pacific $CaCO_3$ preservation and $\delta^{18}O$ since 4 Ma: Paleoceanic and paleoclimatic implications. *Paleoceanography* 6:485–498.
58. Catubig NR, et al. (1998) Global deep-sea burial rate of calcium carbonate during the Last Glacial Maximum. *Paleoceanography* 13:298–310.
59. R Development Core Team (2010) R: A language and environment for statistical computing (R Foundation for Statistical Computing, Vienna, Austria).
60. Gattuso J-P, et al. (2011) seacarb: Seawater carbonate chemistry with R. R package version 3.1.1. Available at https://cran.r-project.org/web/packages/seacarb/index.html.
61. York D, Evensen NM, Martínez ML, Delgado JDB, Derek Y (2004) Unified equations for the slope, intercept, and standard errors of the best straight line least-squares fitting of a straight line. *Am J Phys* 72:367–375.
62. De Boer B, Stocchi P, Van De Wal R (2014) A fully coupled 3-D ice-sheet-sea-level model: Algorithm and applications. *Geosci Model Dev* 7:2141–2156.
63. Archer D (1991) Modeling the calcite lysocline. *J Geophys Res Oceans* 96:17037–17050.
64. Sigman DM, McCorkle DC, Martin WR (1998) The calcite lysocline as a constraint on glacial/interglacial low-latitude production changes. *Global Biogeochem Cycles* 12: 409–427.
65. Robinson RS, et al. (2005) Diatom-bound $^{15}N/^{14}N$: New support for enhanced nutrient consumption in the ice age subantarctic. *Paleoceanography* 20:PA3003.

66. Franois R, et al. (1997) Contribution of Southern Ocean surface-water stratification to low atmospheric CO_2 concentrations during the last glacial period. *Nature* 389:929–935.
67. Robinson RS, Brunelle BG, Sigman DM (2004) Revisiting nutrient utilization in the glacial Antarctic: Evidence from a new method for diatom-bound N isotopic analysis. *Paleoceanography* 19:PA3001.
68. Studer AS, et al. (2015) Antarctic Zone nutrient conditions during the last two glacial cycles. *Paleoceanography* 30:845–862.
69. Duplessy J, et al. (1988) Deepwater source variations during the last climatic cycle and their impact on the global deepwater circulation. *Paleoceanography* 3:343–360.
70. Sarnthein M, et al. (1994) Changes in East Atlantic deepwater circulation over the last 30,000 years: Eight time slice reconstructions. *Paleoceanography* 9:209–267.
71. Sigman DM, Lehman SJ, Oppo DW (2003) Evaluating mechanisms of nutrient depletion and ^{13}C enrichment in the intermediate-depth Atlantic during the last ice age. *Paleoceanography* 18:1072.
72. Lynch-Stieglitz J, et al. (2007) Atlantic meridional overturning circulation during the last glacial maximum. *Science* 316:66–69.
73. Hain MP, Sigman DM, Haug GH (2014) *Treatise on Geochemistry* (Elsevier, Amsterdam), 2nd Ed, Vol 8, pp 485–517.
74. Pena LD, Goldstein SL (2014) Thermohaline circulation crisis and impacts during the mid-Pleistocene transition. *Science* 345:318–322.
75. Shipboard Scientific Party (1999) Leg 177 summary: Southern Ocean paleoceanography. *Proceedings of the Ocean Drilling Program, Initial Reports*, eds Gersonde R, et al. (Ocean Drilling Program, College Station, TX), Vol 177.
76. Powell MJ (1964) An efficient method for finding the minimum of a function of several variables without calculating derivatives. *Comput J* 7:155–162.
77. Brent RP (1973) Some efficient algorithms for solving systems of nonlinear equations. *SIAM J Numer Anal* 10:327–344.
78. Brent RP (2013) *Algorithms for Minimization Without Derivatives* (Prentice-Hall, Englewood Cliffs, NJ).
79. Fletcher R, Reeves CM (1964) Function minimization by conjugate gradients. *Comput J* 7:149–154.

Supporting Information

Chalk et al. 10.1073/pnas.1702143114

SI Sample Locations and Age Model

We present a highly resolved (one sample per 3.5–4.5 ky) δ^{11}B-derived atmospheric CO_2 record from ODP Site 999 (Caribbean Sea; 12°44.64′ N and 78°44.36′ W) (Fig. S1) that spans the 0–260 (i.e., LP260) and 1,080–1,250 ky (i.e., eMPT) time intervals. Sedimentation rates in these intervals are ∼3 cm/ky. Across large parts of the oceans (typically the oligotrophic regions of the low latitudes), the CO_2 content of the gas phase of surface seawater approximately equates to the CO_2 content of the overlying atmosphere (i.e., the surface water is in approximate CO_2 equilibrium with the atmosphere). It is from these locations, such as ODP Site 999 (Fig. S1), that atmospheric CO_2 concentrations can be most reliably reconstructed using the δ^{11}B method (34). Site 999 is today in near air–sea CO_2 equilibrium (approximately +20 μatm) (35) (Fig. S1) and has likely maintained this near-equilibrium state through the Pleistocene and Pliocene (24, 36). The foraminifera at ODP 999 are well-preserved, meaning that diagenesis is not likely to negatively impact our reconstructions. It is also worth noting that even moderate to severe diagenesis has been shown to have little or no impact on the δ^{11}B of planktic foraminifera (37).

For our age model, we generated a benthic δ^{18}O record for ODP Site 999 from ∼600–1,500 ky at a resolution of 3 ky using *Cibicidoides wuellerstorfi* that includes the same samples used to determine CO_2 during our eMPT interval (Fig. S2). The samples were measured on a Finnigan MAT 253 gas isotope ratio mass spectrometer connected to a Kiel IV automated carbonate preparation device at the Zentrum für Marine Tropenökologie. A detailed age model for Site 999 was generated by graphically aligning our benthic foraminiferal δ^{18}O record to the LR04 benthic δ^{18}O stack (29) (Fig. S2) using the Analyseries software (38). For the interval 0–500 ky, we generated a detailed age model by aligning the published planktic foraminiferal (*Globigerinoides ruber*) δ^{18}O record from Site 999 (at ∼0.5- to 2.0-ky resolution) (39) to the LR04 benthic δ^{18}O stack (29) (Fig. S2). The resultant age model provides excellent agreement between our lower-resolution benthic δ^{18}O data and the LR04 benthic δ^{18}O stack in the interval 110–260 ky (Fig. S2).

SI Methodology

Analytical Techniques. Between 140 and 220 individuals of *G. ruber* (white; *sensu stricto*; ∼10 μg per shell) were picked from the 300- to 355-μm size fraction of the coarse (>63 μm) fraction of washed sediments from ODP 999. Foraminiferal samples were cracked and cleaned in the boron isotope clean laboratory at the University of Southampton. The cracking was done between two glass slides under a microscope, and care was taken to open all major chambers to allow for effective clay removal. The cleaning followed established methods for oxidative cleaning (40–42). After cleaning, *G. ruber* samples were dissolved in weak (∼0.15 M) Teflon-distilled nitric acid and separated into two fractions: an "isotope" fraction (90%) and a "trace element" fraction (8–10% of sample volume). Boron was separated from the matrix of the isotope fraction with anion exchange resin (Amberlite IRA-743) in purpose-built columns (22, 43).

Boron isotope ratios were measured at the University of Southampton on a Thermo Scientific Neptune multicollector inductively coupled plasma mass spectrometer following established methodology (21, 36, 42, 43). External reproducibility was calculated based on the reproducibility of an in-house standard [Japanese coralline *Porites* – JCP-1 = 24.2‰ (42)] described by Eq. **S1** below, where [^{11}B] = intensity in volts of ^{11}B; for this study, the 2σ uncertainty typically corresponds to ∼0.2‰:

$$2\sigma = 1.87\cdot\exp^{-20.6\left[^{11}B\right]} + 0.22\cdot\exp^{-0.43\left[^{11}B\right]}. \quad \textbf{[S1]}$$

The trace element fraction was diluted, and Me/Ca ratios of Li, B, Na, Mg, Al, Mn, Fe, Sr, Cd, Ba, Nd, and U were measured on a Thermo Scientific Element 2-XR inductively coupled plasma mass spectrometer at the University of Southampton. Over the period of this study, reproducibility of three internal standards with a range of Me/Ca ratios was 4% for Mg/Ca and 5% for Al/Ca. We use the trace element data to screen for diagenesis and other potential artifacts. Samples with Al/Ca > 100 μmol/mol were strictly removed to preserve data quality, and we find no anomalies in other element ratios (e.g., Mn/Ca, Ba/Ca, and Fe/Ca).

Mg/Ca temperatures were calculated following the approach of Evans and Müller (44) and using an Mg/Ca of seawater (Mg/Ca_{sw}) that was calculated from the modeled study of Fantle and DePaolo (45). We use an H value of 0.41, although species-specific to *Trilobatus* (formerly *Globigerinoides*) *sacculifer* (46), as no calibrated H value for *G. ruber* is currently available. Note that the accuracy of this reconstruction is not crucial to our findings, since sea surface temperature has a relatively weak effect on calculated CO_2 (*Determination of CO_2 from δ^{11}B-Derived pH*), and also, the potential change in Mg/Ca_{sw} over the last million years is small because of the long residence times of the elements involved.

Determination of pH from δ^{11}B of *G. ruber*. Boron is present in two principal forms in seawater: boric acid [$B(OH)_3$] and borate ion [$B(OH)_4^-$]. The relative proportion of these two species depends on pH and the dissociation constant for boric acid, pK^*_B:

$$\log_{10}\frac{B(OH)_4^-}{B(OH)_3} = pH - pK_B^*. \quad \textbf{[S2]}$$

An isotopic fractionation between the two stable isotopes of boron-11 (∼80% abundance) and boron-10 (∼20%) is also associated with this equilibrium (above), as the bond strengths between boron and the hydroxyl ion in boric acid and the borate ion differ. The ^{11}B concentrates in the more strongly bonded boric acid, giving it a higher δ^{11}B than the borate ion by ∼27.2‰ (47). The delta notation (δ^{11}B) is used to express differences in boron isotope ratios:

$$\delta^{11}B(‰) = \left[\left(\frac{\frac{^{11}B}{^{10}B_{smp}}}{\frac{^{11}B}{^{10}B_{ref}}}\right) - 1\right]\times 1{,}000, \quad \textbf{[S3]}$$

where $^{11}B/^{10}B_{ref}$ is the isotopic ratio of NIST SRM 951 boric acid standard ($^{11}B/^{10}B = 4.04367$) (48) and $^{11}B/^{10}B_{smp}$ is the isotopic ratio of the sample. The basis of the boron isotope–pH proxy is that, because the borate ion is tetrahedral and charged, it is more readily substituted into $CaCO_3$ (49, 50). Therefore, we can solve for pH based on the reconstructed isotopic composition of $\delta^{11}B_{borate}$:

$$pH = pK_B^* - \log\left(-\frac{\delta^{11}B_{sw} - \delta^{11}B_{borate}}{\delta^{11}B_{sw} - (\alpha\cdot\delta^{11}B_{borate}) - 1{,}000\cdot(\alpha - 1)}\right), \quad \textbf{[S4]}$$

where pK^*_B is the dissociation constant for boric acid at reconstructed in situ temperature, salinity, and pressure (51); $\delta^{11}B_{sw}$ is the isotopic composition of seawater (39.61‰) (52); $\delta^{11}B_{borate}$ is the isotopic composition of borate ion; and α is the isotopic fractionation factor between the two aqueous species of boron in seawater (α = 1.0272, equivalent to an equilibrium isotope fractionation of ~27.2‰) (47). Boron is well-mixed in the oceans, with a residence time of 10–20 My; to account for likely (small) changes in the boron isotopic composition of seawater ($\delta^{11}B_{sw}$), we use a simple linear extrapolation with a central value at modern $\delta^{11}B_{sw}$ (39.61 ± 0.1‰) (52) with uncertainty increasing by ±0.12‰ by 1,200 ky (0.1‰/My). This central value is consistent with an independent constraint, and any possible changes (53–55) are well-accounted for by the generous uncertainties that we ascribe to all parameters.

As $\delta^{11}B_{ruber}$ (the $\delta^{11}B$ of boron in *G. ruber* calcite) is offset from $\delta^{11}B_{borate}$, it is necessary to first account for this relatively minor deviation to calculate pH from $\delta^{11}B_{ruber}$, and a size-specific core top, culture, and field measurement calibration (Eq. **S5**) is applied for $\delta^{11}B_{borate}$ reconstruction (33, 39). This relationship has been shown in other studies to provide for accurate atmospheric CO_2 reconstructions (1, 21, 23). Uncertainties in this calibration (*G. ruber* 300–355 μm) are propagated through all relevant calculations (shown below at 2σ):

$$\delta^{11}B_{borate} = \frac{(\delta^{11}B_{ruber} - 8.87 \pm 1.51)}{0.6 \pm 0.08}. \quad \textbf{[S5]}$$

Determination of CO_2 from $\delta^{11}B$-Derived pH. To calculate aqueous CO_2 from pH, a second carbonate system parameter is required (34). Here, we briefly outline two approaches to estimate total alkalinity (ALK) to derive CO_2 from our pH data: (*i*) ALK remained within a specified range of its modern value, and (*ii*) ALK change correlates with reconstructed pH change. Below, we describe why both approaches yield very similar results, and we describe a sensitivity test to show that our main conclusions are not affected by the choice of how to estimate ALK. In the main text and our tabulated dataset, we assume that ALK has remained within a generous range around its modern value (~2,330 ± 175 μmol/kg) over the investigated period. The outcome of our own model inversion of CO_2 change of the last 1,500 ky (*Model Inversion* has details on the model) suggests a total ALK range of only 130 μmol/kg, much less than the 350-μmol/kg uncertainty range propagated here. This means that we fully explore the likely ALK range based on modeling of whole-ocean ALK variability on G-IG timescales and over the last 1,500 ky (1, 26). This treatment of the second carbonate system parameter essentially assumes that any change in ALK will drive the majority of its impact on CO_2 by changing pH (which we reconstruct directly) rather than by changing the abundance of carbonate and bicarbonate ions. This assertion is based on first principle carbon chemistry and can be verified by comparing reconstructed pH with the ice core CO_2 record (Fig. S3*A*). When we cross-plot $\delta^{11}B$-based pH against ice core CO_2, we find that the data are well-described by the theoretical pH to CO_2 relationships, assuming either constant DIC or constant ALK (Fig. S3*A*), in support of our assertion. The alternative view is that much of the reconstructed pH change was caused by changes in ALK, such that ALK and pH are correlated (i.e., the ~0.2 pH increase during the Last Glacial Maximum corresponds to a +100-μmol/kg ALK increase) (26, 56). We carry out a sensitivity test to estimate how much difference in terms of CO_2 that it makes to account for this correlation (Fig. S3*B*). We find that including the ALK to pH correlation reduces our estimate for additional glacial-stage CO_2 reduction by about 5 μatm, and it reduces our estimated increase of the G-IG CO_2 range by about 5 μatm (Fig. S3*C*). As described above, this relatively modest change is because of the fact that ALK change causes most of its impact on CO_2 by changing surface pH, the parameter that we reconstruct (Fig. S3*B*). We argue that the modest difference between the two ALK assumptions does not change the main conclusions of this study, especially given the agreement between our data, previously published fully independent CO_2 reconstructions, and our carbon cycle modeling results (Fig. 4 and Fig. S4). Since the ALK to pH correlation is itself uncertain, we prefer the calculation using a large and constant ALK uncertainty range that more than covers existing estimates of G-IG ALK change (26, 56). With this approach, the small deviation between the ALK assumptions is effectively covered by our uncertainty propagation, and there is little independent evidence to suggest that this assertion is invalid (57, 58).

Using $\delta^{11}B$-derived pH and the prescribed ALK and modern aqueous CO_2 disequilibrium, uncertainties are propagated via a Monte Carlo simulation (n = 10,000) in the statistical analysis program R (59), and 95% confidence intervals are calculated from the variation within these simulations. Two SD uncertainties on the individual input variables are included for $\delta^{11}B$ (with or without analytical uncertainty defined by Eq. **S1**, normal distribution), Mg/Ca-derived temperature (±3 °C, normal distribution), salinity (±3 psu, normal distribution), ALK (±175 μmol/kg, uniform distribution), and $\delta^{11}B_{sw}$ (39.61 ± 0.10–0.22‰, normal distribution) (52). Atmospheric CO_2 was then calculated from aqueous CO_2 using Henry's Law, subtracting the modern extent of disequilibria with respect to CO_2^{atm} at the site [given a nominal uncertainty at 2σ of ±50% (i.e., ±10 μatm)]. Uncertainties in CO_2 also include propagation of the uncertainties in the $\delta^{11}B$ calibration of *G. ruber* (Eq. **S5**). All subsequent carbonate system calculations in R were performed using the seacarb package (59, 60).

SI Forcing to SL Relationship

Extraction of the underlying relationship between two empirical datasets requires careful consideration of uncertainty in both x and y coordinates (61). In our case, the x coordinate is CO_2 climate forcing, ΔR_{CO2}, which is calculated directly from reconstructed CO_2 following ref. 33:

$$\Delta R_{CO2} = \alpha \times \ln\frac{CO_2}{CO_2^o}; \alpha = 5.35\frac{W}{m^2}; CO_2^o = 278\ \mu atm. \quad \textbf{[S6]}$$

We calculate mean and SD of ΔR_{CO2} as the half-point and quarter-width of the ±2σ interval of our CO_2 reconstruction. As for the y coordinate, SL in our case, we point out that there are three sources of uncertainty: (*i*) the inherent uncertainty of the SL estimate documented alongside each SL record, (*ii*) the range of SL within the age window defined by the relative age uncertainty of the SL and the CO_2 age models, and (*iii*) the systematic discrepancies between different SL records. The latter point we address by carrying out our analyses independently for a number of recent SL records (11, 12, 24, 62), and we find only modest differences, suggesting that our conclusions are robust to these systematic SL discrepancies. To account for both *i* and *ii*, for each CO_2 data point, we estimate SL and its uncertainty by constructing the cumulative distribution function (CDF) of all SL data that fall within the relative age uncertainty window (which we take to be 1.5–2 ky for our LP260 data; an uncertainty ramps from 2 to 4 ky over the course of the 800-ky compilation of ice core CO_2 reconstructions and 6 ky for our eMPT data). For each individual CDF, we estimate the appropriate SL mean and SD as the half-point and half-width of the 16 to 84% interval (corresponding to ±1σ). This procedure yields typical individual data point SL uncertainties about 20 m (±2σ) and significantly larger uncertainties for a few points that happen to correspond to times of rapid SL change.

As for the regression of the underlying CO_2 forcing to SL relationship, we make use of the approach laid out by York et al. (61), a generalized form of "reduced major axis" regression method that takes full account of normal error in x and y. We carry out this regression technique using four independent SL reconstructions (11, 12, 24, 62) for both our LP260 CO_2 dataset (Fig. S7*A*) and our eMPT dataset (Fig. S7*D*). In all cases, we display the regression confidence interval. The confidence intervals of the regressed slopes for LP260 (Fig. S7*B1*) and eMPT (Fig. S7*B3*) are of particular interest. We consistently find the CO_2 forcing to SL slope to be significantly steeper during LP260 (about 40–50 m/Wm^{-2}) than during eMPT (less than 25 m/Wm^{-2}), supporting the main line of argument in our study.

To build confidence in our regression method, we offer three tests. (*i*) Are the regressions based on our LP260 dataset consistent with regressions based on the compilation of the continuous ice core CO_2 record of the last 800 ky? (*ii*) Does preindustrial SL fall within the prediction interval of our regressed CO_2 forcing to SL relationships? (*iii*) Is the regression method by York et al. (61) skillful in extracting the correct CO_2 forcing to SL relationships when put to the test with synthetic data that mimic our eMPT data and their uncertainties?

To address *I*, we carry out the regression using the ice core CO_2 record against all SL records based on a 200-ky sliding window of data. Because the sampling interval of the ice core CO_2 compilation changes dramatically over its 800-ky range (and in particular, over the course of the last deglaciation), we regularize the CO_2 data by binning it into ±1-ky increments and estimate bin mean and SD analogous to the SL data. We find that, throughout the last 800 ky, the CO_2 forcing to SL slopes regressed in that way generally fall within a band of 35–55 m/Wm^{-2} (gray shading in Fig. S7*B2*), in good agreement without LP260 data and significantly greater than for our eMPT data. We note that the slope regressed from the SL record that is based on Mg/Ca–$\delta^{18}O$ deconvolution (11) exhibits a long-term oscillation not seen in any of the other SL regressions, but even at its lowest point, it is still significantly larger than that regressed during the eMPT. Likewise, while the Mediterranean SL reconstruction (12) falls into a constant narrow range for most of the 800 ky, its regressed CO_2 forcing to SL slope yields anomalous variability during a brief interval around 500 ky, where the SL record is known to be overprinted by a series of sapropel layers. The regression based on the Red Sea SL record (25), arguably the best constrained SL reconstruction, is remarkably constant over the entire 500-ky period that it spans, as is the case for the entire last 800 ky for the regression based on simulated SL by De Boer et al. (62). Based on that analysis, we conclude that there is no evidence for substantial changes in the CO_2 forcing to SL slope over the entire 800-ky duration of the ice core CO_2 record and that the significantly lower regressed slopes for our eMPT dataset therefore speak to a change in the CO_2 forcing to SL relationship associated with the MPT. Furthermore, we note that, in Fig. 2, we only present the regression results of the Mediterranean SL record, which this supplementary analysis suggests to be both robust and the most conservative record covering both the LP260 and eMPT intervals. We have further confidence in our conclusion of an MPT reduction in the CO_2 forcing to SL slope, because we find an equivalent change when considering the LR04 benthic foraminifera $\delta^{18}O$ stack instead of SL (Fig. S8), which is observationally well-constrained and carries a significant component SL signal.

To address *ii*, the test for SL predicted for preindustrial CO_2 forcing, we replicate our analysis of the CO_2 forcing to SL slope for the intercept regression parameter, shown in an analogous way in Fig. S7*C*. When using the regressed CO_2 forcing to SL relationship, however, it is the prediction interval (dashed in Fig. S7*C*) and not the regression confidence interval that is relevant, because the CO_2 forcing to SL regression does not embody residual SL change caused by factors, such as orbital change. Hence, the prediction interval at the intercept is wider than the intercept confidence interval, and it comfortably includes preindustrial SL at preindustrial CO_2 forcing during LP260.

Finally, to address *iii*, the question as to the skill of York regression to extract the correct CO_2 forcing to SL slope even in the face of substantial x and y uncertainty of individual points and an overall low signal to noise ratio, we construct a synthetic test that mimics the signal to noise ratio of our eMPT data (Fig. S9). That is, we presuppose a known CO_2 forcing to SL relationship and generate randomized data points based on the typical uncertainties of CO_2 forcing and SL. To carry out this analysis, we change the number of synthetic data points used for the regression and find that (*i*) the true slope of the known synthetic relationship falls within the regressed slope confidence interval; (*ii*) the width of the regressed slope confidence interval systematically narrows as the number of data points increases; and (*iii*) at 50 data points, the slope confidence interval is narrow enough to detect the change in slope that we reconstruct between LP260 and eMPT.

SI Carbon Cycle Modeling

Model Details. To simulate the global carbon cycle and atmospheric CO_2 levels across the MPT, we make use of the recently updated CYCLOPS model (27). The model represents the oceanic carbon cycle and physical circulation as the exchange between 18 separate surface, middepth, and deep water reservoirs, as well as carbon fluxes between surface water reservoirs and an atmospheric reservoir. Following previous work (63, 64), the model simulates the open system $CaCO_3$ cycle through explicit representation of undersaturation-driven seafloor dissolution of biogenic $CaCO_3$ rain that originates from the surface.

To simulate global carbon cycle variations in the Pleistocene, we apply three fully separate forcings to the model, all of which represent well-established modes of carbon cycle and circulation change previously investigated using CYCLOPS: (*i*) major nutrient drawdown driven by glacial-stage iron fertilization of the Sub-Antarctic Zone of the Southern Ocean (7, 65); (*ii*) coupled glacial-stage reduction in vertical exchange, export production, and residual surface nutrient status of the Polar Antarctic Zone of the Southern Ocean (56, 66–68); and (*iii*) glacial-stage shoaling of the AMOC (69–72). The rationale and evidence base for these changes have been reviewed elsewhere (73), and the model's atmospheric CO_2 sensitivity to these mechanisms has been evaluated in detail (27). To represent the time evolution in model forcing, we use ODP 1090 iron mass accumulation rate (1), ODP 1094 Ba/Fe (28), and ODP 982/U1313 (29, 30) observational records to adjust model conditions in the Sub-Antarctic Zone, the Polar Antarctic Zone, and the global deep water circulation pattern, respectively. Other drivers of CO_2 change (e.g., silicate weathering feedback, temperature) are not considered here but will be investigated in the future. Similarly, by implementing Atlantic circulation changes based on North Atlantic carbon isotope gradients, our model does not reflect exceptional circulation weakening during MIS 23 inferred from neodymium isotopes (74) or any other modes of AMOC reorganization.

Extension of ODP 1094 Ba/Fe Proxy Forcing. The previously published ODP 1094 Ba/Fe record from 0 to 1 Mya was extended to allow us to start the forced simulation as early as 1.5 My. The composite section for the deeper part of ODP core 1094 (>121 mcd; 1–1.5 My) was mainly reconstructed using magnetic susceptibility (75), Fe counts derived from X-ray fluorescence (XRF) scanning on sediments of Holes A and D, and the $\delta^{18}O$ of the planktonic foraminiferal species *Neogloboquadrina pachyderma*. The age model of the core is based on tuning the $\delta^{18}O$ of the benthic foraminifer *C. wuellerstorfi* to the LR04 benthic stack

(29), as will be documented elsewhere. Oxygen isotope analyses were performed with a Thermo GasBench II coupled to a Thermo Delta V Plus mass spectrometer at the Geological Institute, ETH Zurich (1σ error of 0.07‰). The relative sedimentary concentrations of Ba and Fe were acquired with an AVAATECH profiling XRF core scanner at the MARUM, University of Bremen using the same settings and procedures as in ref. 28 but with a different detector (Canberra X-PIPS Silicon Drift Detector, Model SXD 15C-150-500). To assure that the XRF data are consistent throughout the entire record, four sections between 0 and 1 My have been rescanned. The elemental XRF data of the rescanned sediments are correlated to each other, and their linear fit is used to scale newly acquired data accordingly ($r = 0.97$ for Fe, $r = 0.77$ for Ba).

Model Inversion. The relationship between the observational records and the forcing applied to the model (sub-Antarctic nutrient status, polar Antarctic/deep Southern Ocean exchange, polar Antarctic surface nutrient status, and Atlantic overturning) is represented as four equations with a total of seven free parameters (i.e., intercept and slope, threshold in the case of Atlantic overturning). The Atlantic circulation is simulated as "shallow" only if the reconstructed vertical stable carbon isotope gradient in the deep North Atlantic increases above a threshold value determined as part of the inversion; all other forcing functions are continuous and monotonic. For the Antarctic changes, vertical exchange scales with Ba/Fe, while surface nutrient status scales with the square root of Ba/Fe, thereby in effect, assuming a sublinear scaling between Ba/Fe and export production [i.e., the property arguably recorded by Ba/Fe at ODP 1094 (28)]. The seven forcing function parameters are initially set to arbitrary (but sensible) values.

We invert the model by finding the specific combination of the seven forcing function parameters that minimize the rms error of simulated atmospheric CO_2, as evaluated against a composite reconstruction of atmospheric CO_2 from Antarctic ice cores (19). That is, given the observational forcing records, the forward model, and the CO_2 record, we invert to obtain the model forcing parameters that minimize the rms objective function. To be confident in the outcome of the minimization procedure across 7D parameter space, we incorporate into the model two fully independent methods and verify that they converge onto the same solution: (*i*) Powell's conjugate direction method (76–78) and (*ii*) the Fletcher–Reeves implementation of the Steepest Descent conjugate gradient method (79). Side conditions relating to physically possible parameter solutions are encoded directly into the model, and both algorithms converge to the same solution at an rms of 12.2 μatm.

SI Quantification of $^{G}CO_2$, $^{IG}CO_2$, and $^{IG\text{-}G}\Delta CO_2$

Given our two δ^{11}B-based CO_2 reconstructions (eMPT, LP260), we wish to (*i*) quantify by how much glacial and interglacial CO_2 levels (i.e., $^{G}CO_2$ and $^{IG}CO_2$, respectively) are different across the MPT and by how much the magnitude of G-IG CO_2 cycles (i.e., $^{IG\text{-}G}\Delta CO_2$) has changed and (*ii*) compare our estimates with equivalent estimates derived from existing CO_2 records (1, 2, 19) as well as from our model-derived predictions of CO_2 (*SI Carbon Cycle Modeling*). This section describes the details of the analysis and offers discussion of the rationale behind these calculations. Our analysis of the CO_2 datasets consists of four steps: (*i*) define which individual data points represent glacial conditions and which data points represent interglacial conditions, (*ii*) estimate the average CO_2 and its uncertainty from the two sets (i.e., $^{G}CO_2$ and $^{IG}CO_2$) of CO_2 data, (*iii*) estimate the G-IG CO_2 difference (i.e., $^{IG\text{-}G}\Delta CO_2$) before and after the MPT, and (*iv*) test whether the resulting changes are statistically significant.

To define which individual data points contribute, we subsample each record based on a percentile cutoff criterion using, for example, only the 25% "most interglacial" and the 25% "most glacial" data points in the quantification of $^{G}CO_2$, $^{IG}CO_2$, and $^{IG\text{-}G}\Delta CO_2$. In the case of the δ^{11}B-based CO_2 reconstructions, we can rank the individual data points based on δ^{18}O measured on the same sample to directly reflect climate state, but in the case of the direct ice core measurements and our model-simulated CO_2, we have to rank the individual data points based on their CO_2 level. The value of 25% for the cutoff criterion is arbitrary, and therefore, we carry out and present the analysis for the full 1–50% range of nonoverlapping subsamples (Fig. S4). A low percentile cutoff implies that only the few most extreme data points are subsampled as glacial and interglacial, which maximizes the glacial/interglacial difference but also leads to a relatively large uncertainty, because only few data contribute to the estimates. Conversely, a high percentile cutoff implies that more individual data contribute to the estimation of CO_2, which reduces the uncertainty and increases robustness but also, progressively averages away the end member changes that we try to quantify. For brevity, we make the tradeoff between robustness and sensitivity and exclusively discuss the 25% percentile cutoff in the main text, and we note that our qualitative results are independent of that choice (Fig. S4).

The second step of our analysis is to estimate $^{G}CO_2$ and $^{IG}CO_2$ based on their respective subsamples (see above) and also propagate the uncertainty of the individual data points. To this end, we first sum up and normalize the probability density functions of the individual data points and their normally distributed uncertainty. We assign 1σ uncertainties of 20 μatm to our CO_2 data, 14 μatm to the Hönisch et al. (11) data (ref. 1 as published; we note that ref. 1 does not include a number of sources of uncertainty that are included in the uncertainty calculations for our data), a nominal 10 μatm to ice core data, and 12.2 μatm to simulated CO_2 based on model inversion residual rms. From these cumulative subsample probability density functions, we estimate the central tendency as the median probability and that normal dispersion as one-half of the central 66% cumulative probability interval. Thus, the dispersion of our estimates represents a combination of inherent measurement uncertainty associated with individual data points and of the true spread in CO_2 levels within the subsample. To estimate $^{IG\text{-}G}\Delta CO_2$, we simply subtract the central estimate of $^{G}CO_2$ from $^{IG}CO_2$, whereby the normal dispersion of $^{IG\text{-}G}\Delta CO_2$ is propagated as the root sum of squares of the normal dispersion estimates of $^{G}CO_2$ from $^{IG}CO_2$.

The final step in our analysis is to evaluate the significance of the differences that we find in glacial and interglacial CO_2 and glacial/interglacial CO_2 range before and after the MPT (i.e., $\Delta^{G}CO_2$, $\Delta^{IG}CO_2$, and $\Delta^{IG\text{-}G}\Delta CO_2$ as also visualized in Fig. 4). To this end, we subtract eMPT $^{G}CO_2$, $^{IG}CO_2$, and $^{IG\text{-}G}\Delta CO_2$ from the corresponding LP260 estimates, again propagating the estimate dispersion as the root sum of squares of the individual normal dispersion estimates. For all four CO_2 datasets (i.e., two δ^{11}B-based CO_2 records, ice core data, and model inversion results), we find that estimated $\Delta^{IG}CO_2$ falls onto zero within its 1σ dispersion (thick black whisker in Fig. 4), and thus, we cannot reject the null hypothesis that interglacial CO_2 levels were identical during our intervals (eMPT and LP260). Conversely, we find that estimated $\Delta^{G}CO_2$ is negative for all four CO_2 datasets, with the deviation from zero exceeding the threshold of 1.64 σ for one-sided testing (thin black whisker in Fig. 4). That is, we can reject at 95% confidence level that glacial-stage CO_2 before the MPT was as low or lower than after the MPT. Likewise and largely driven by this significant glacial-stage CO_2 decline across the MPT, the estimated MPT change in the G-IG CO_2 range is significantly greater than zero for all four datasets (at 95% confidence level for one-sided testing) (thin black whisker in Fig. 4). Thus, we can reject at 95% confidence level the null hypothesis that the magnitude of glacial/interglacial CO_2 change before the MPT was as large (or larger) as the glacial/interglacial CO_2 change after the MPT.

Additional results of statistical analysis are tabulated in Table S1.

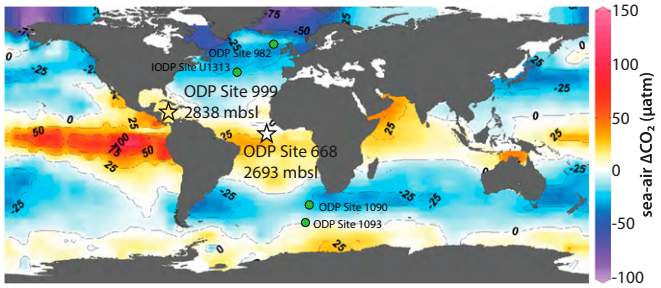

Fig. S1. Map of sediment core sample sites. Color scale represents CO_2 disequilibrium between surface water and air, with surface water supersaturation indicated by red tones (35). The locations of ODP 999 and ODP 668 are indicated. Also indicated are the locations of cores used to inform our modeling results in green: ODP 982, IODP U1313, ODP 1090, and ODP 1093.

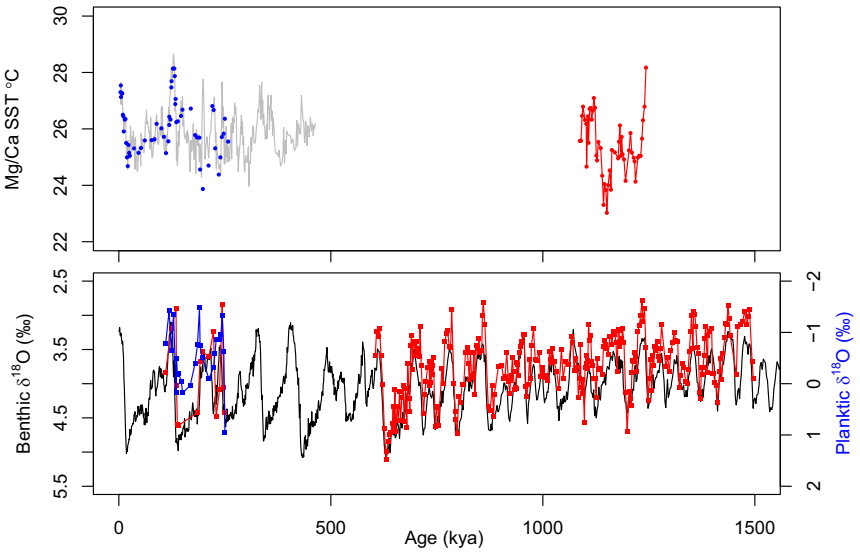

Fig. S2. Foraminiferal Mg/Ca and oxygen isotope measurements from ODP 999. (*A*) Planktic Mg/Ca temperature estimated from *G. ruber* (blue, LP260; red, eMPT). Temperatures are calculated as stated in *Analytical Techniques*; also shown is the previous record of Mg/Ca sea surface temperature (SST) from this Site (gray) (39). (*B*) Planktic *G. ruber* (blue) and benthic *C. wuellerstorfi* (red) oxygen isotope results plotted vs. the global benthic foraminiferal oxygen isotope stack (black) (29).

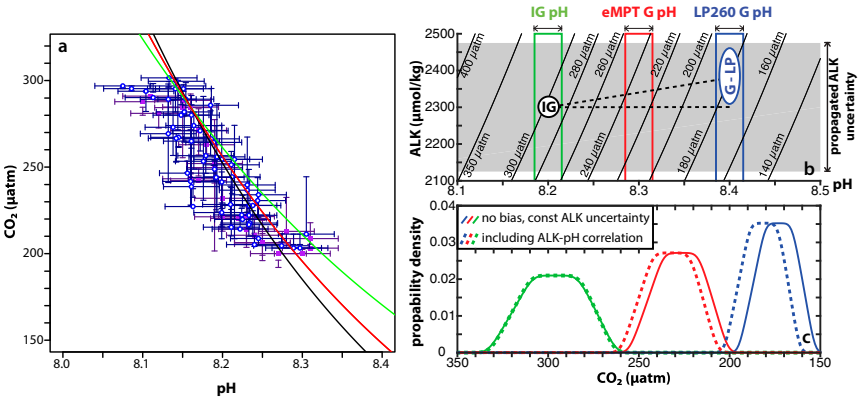

Fig. S3. Assessment of ALK assumption. Our treatment of the second carbonate system parameter asserts that any change in ALK will cause most of its CO_2 impact by changing pH, which we reconstruct directly, rather than by the change in the abundance of carbonate and bicarbonate ion. (*A*) To test this assertion, we cross-plot reconstructed pH and ice core CO_2 and assess the relationship between these empirical data against our assertion. Blue and purple dots are our LP260 CO_2 data and CO_2 data from ref. 1, respectively, with the corresponding CO_2 interpolated from the ice core CO_2 record (19). The three solid lines represent the theoretical pH–CO_2 relationships under the following assumptions: (red) constant DIC, (black) constant ALK, and (green) DIC and ALK both change with a set ratio of 1:1. Either assumption of constant dissolved inorganic calcite (DIC) or constant ALK gives faithful reproduction of ice core CO_2 from the Site 999 and 668 δ^{11}B–pH records, in strong support of our assertion. The CO_2 uncertainty in the empirical data relates to the age model uncertainty (~2 ky) of the pH data points and the resulting spread in interpolated ice core CO_2. (*B*) To illustrate our ALK assumption further, we show CO_2 as a function of ALK and pH at 25 °C and salinity of 35, as predicted yielding nearly vertical contours that show a strong sensitivity of CO_2 to pH and a weak sensitivity to ALK. As a point of reference, we highlight pH values of 8.2 ± 0.15, 8.3 ± 0.15, and 8.4 ± 0.15 to represent interglacial pH values during both eMPT and LP260, eMPT glacial pH, and LP260 glacial pH, respectively. The large ALK uncertainty range that we propagate in our calculations (gray shading) more than covers estimates of ALK change over recent G-IG cycles (i.e., dashed line connecting IG with Last Glacial Maximum). (*C*) From the sensitivity calculations, we estimate the CO_2 offset between two plausible treatments of ALK uncertainty: (solid lines) assuming ALK remained within constant range (i.e., ±175 µmol/kg) and (dashed lines) assuming an ALK to pH correlation of +100 µmol/kg per 0.2 pH increase in addition to the ±175 µmol/kg ALK uncertainty. We find that the ALK to pH correlation causes modest mean increases of ~5 and ~8 ppm in the estimates for eMPT and LP260 glacial CO_2 levels, respectively. The implied ~3-ppm reduction in the difference between glacial-stage eMPT and LP260 CO_2 is too small to undermine the main conclusions of our study.

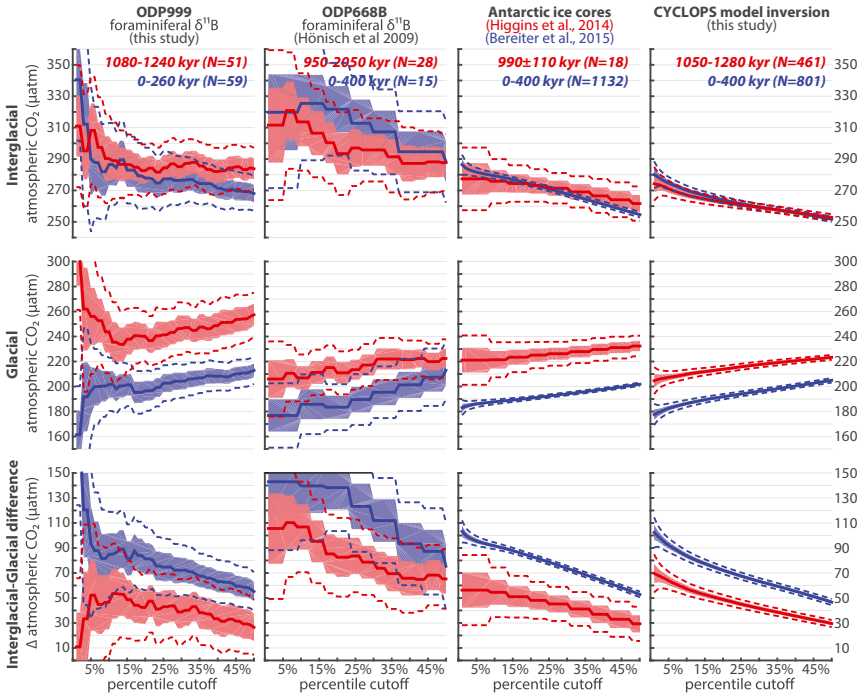

Fig. S4. Quantification of CO_2 change since the MPT. As described in detail in *Materials and Methods*, we quantify (*Top*) interglacial CO_2, (*Middle*) glacial CO_2, and (*Bottom*) interglacial – glacial CO_2 for data both from the latest Late Pleistocene (blue) and during or before the MPT (red). From left to right, quantification is carried out on four different datasets: boron isotope data from ODP 999 (this study) and ODP 668B (1), CO_2 directly measured on air trapped in Antarctic ice using the compilation of continuous ice core CO_2 reconstructions (19) and stratigraphically disturbed ~1-My-old "blue ice" from the Allan Hills (2), and CYCLOPS model inversion (this study). To define glacial and interglacial subsets of the datasets, we use on a cutoff criterion, subsampling the data with a given percentile of lowest/highest δ^{18}O (marine records) or CO_2 (ice core, model). For this figure, we carry out this analysis while systematically changing the value of the critical percentiles (*x* axis). The results discussed in the main manuscript and shown in Fig. 4 correspond to a 25% cutoff percentile, but as shown here, our conclusions are robust across a wide range of percentiles. The underlying data are compiled for percentile increments of 5% in Table S1.

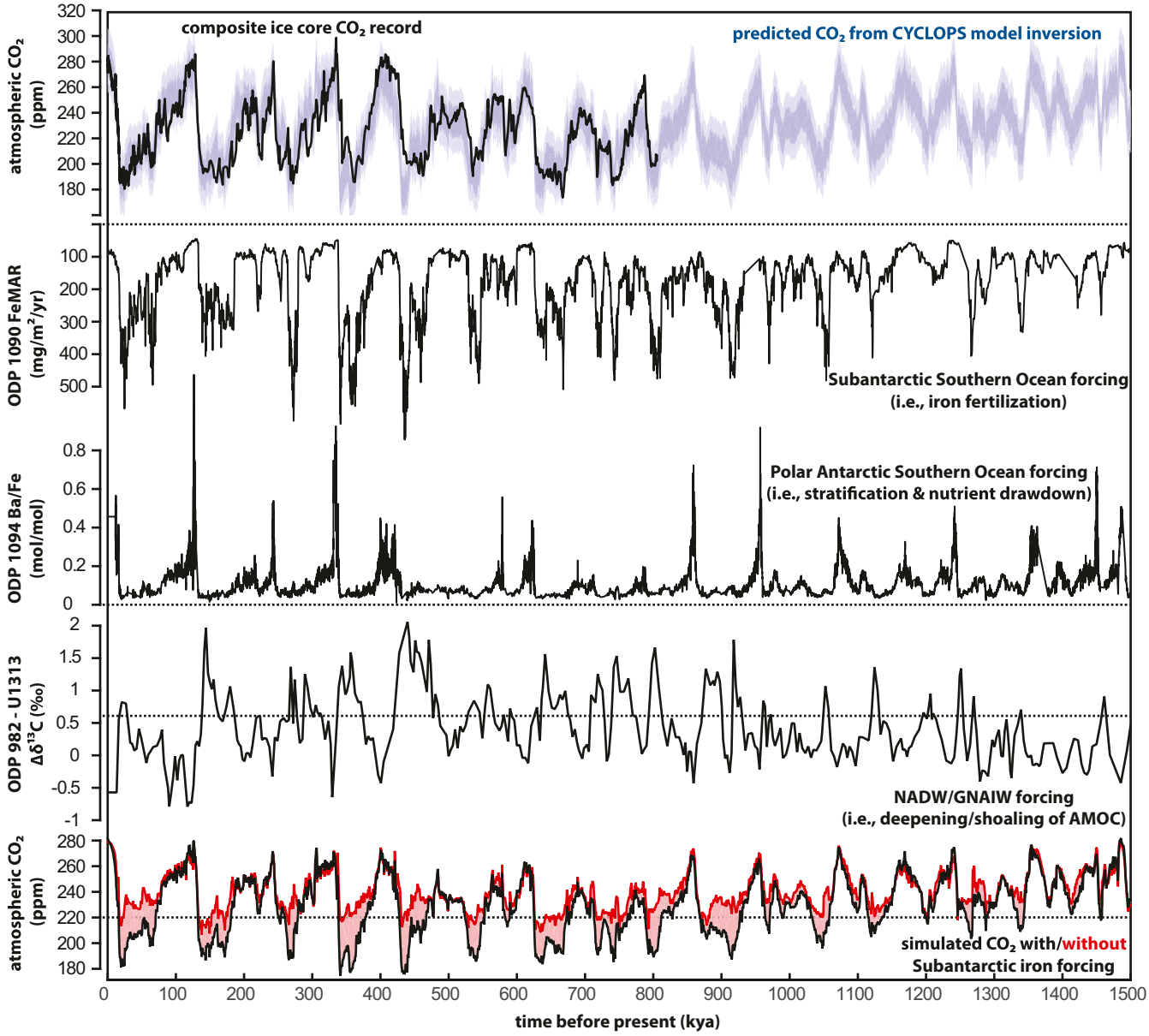

Fig. S5. Overview of CYCLOPS model inversion results. *Top* shows (in black) the composite ice core CO_2 record (19) used as the inversion target and (in blue) the model inversion result, with dark and light shading indicating $\pm 1\times$ and $\pm 2\times$ the rms error of the inversion (12.3 μatm), respectively. *Middle* shows the three paleoceanographic proxy records used to drive the inversion as described in detail in *SI Carbon Cycle Modeling*. *Bottom* illustrates the contribution of dust-borne iron fertilization of the Sub-Antarctic Zone of the Southern Ocean, highlighting the simulated CO_2 change that can be attributed to that forcing. FeMAR, iron mass accumulation rate; NADW/GNAIW, North Atlantic Deep Water/Glacial North Atlantic Intermediate Water.

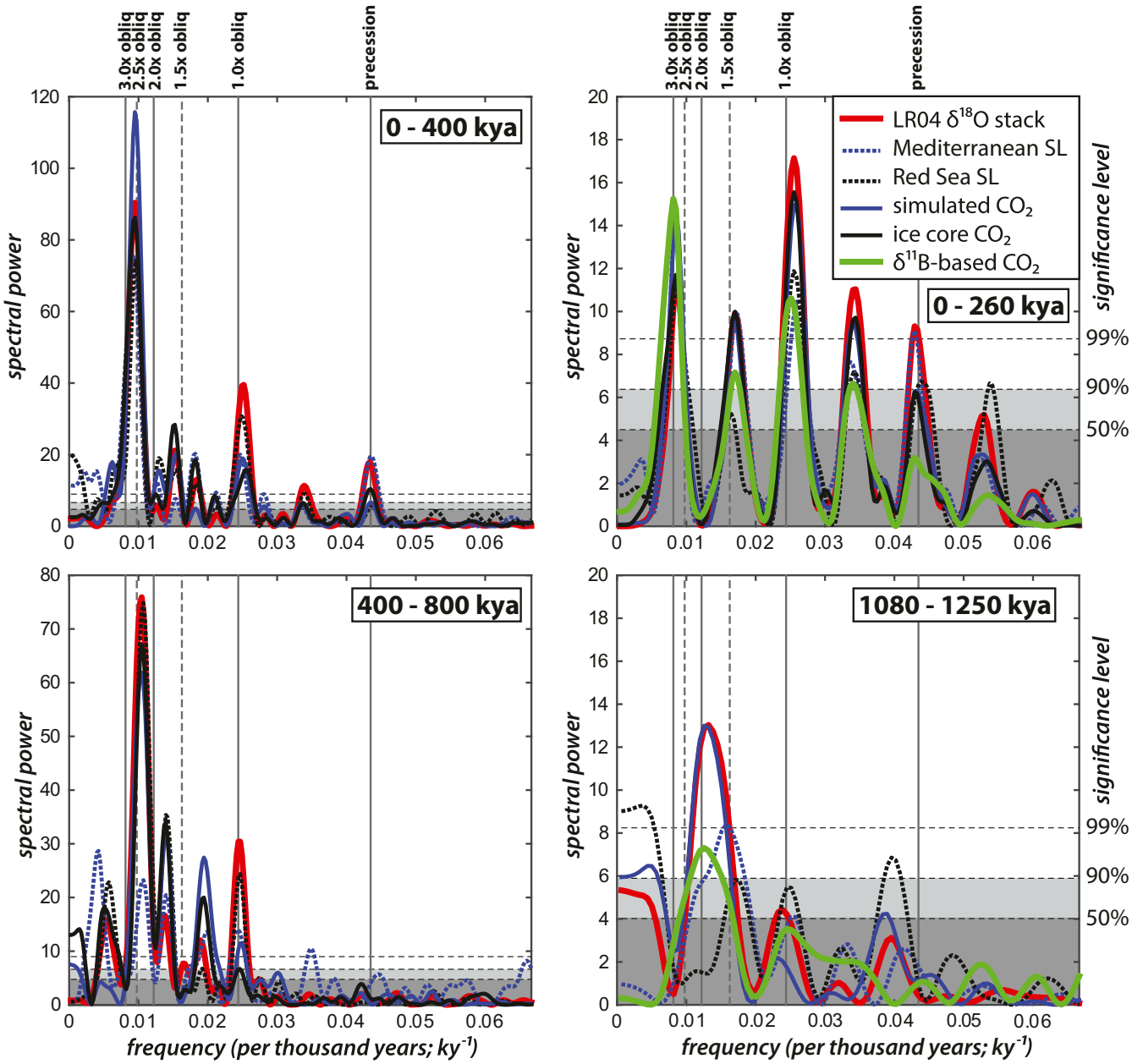

Fig. S6. Spectral analysis of various paleoclimatological records. Ice core CO_2 levels (19), benthic foraminiferal oxygen isotope stack (29), reconstructed SL change (12), our boron isotope-derived CO_2 reconstruction, and CO_2 calculated by inversion of the CYCLOPS carbon cycle model (as described in *SI Carbon Cycle Modeling*). Spectra in *Left* are derived from data down-sampled to the temporal resolution of the oxygen isotope stack, and spectra in *Right* are derived from data down-sampled to the temporal resolution of our boron isotope-derived CO_2 reconstruction. Evaluating the datasets at identical age points yields identical critical significance levels (horizontal dashed lines), shown here for 0.5, 0.9, and 0.99 for all panels. We use the Lomb–Scargle method for frequency analysis of unequally spaced data as implemented in the "plomb" Matlab function.

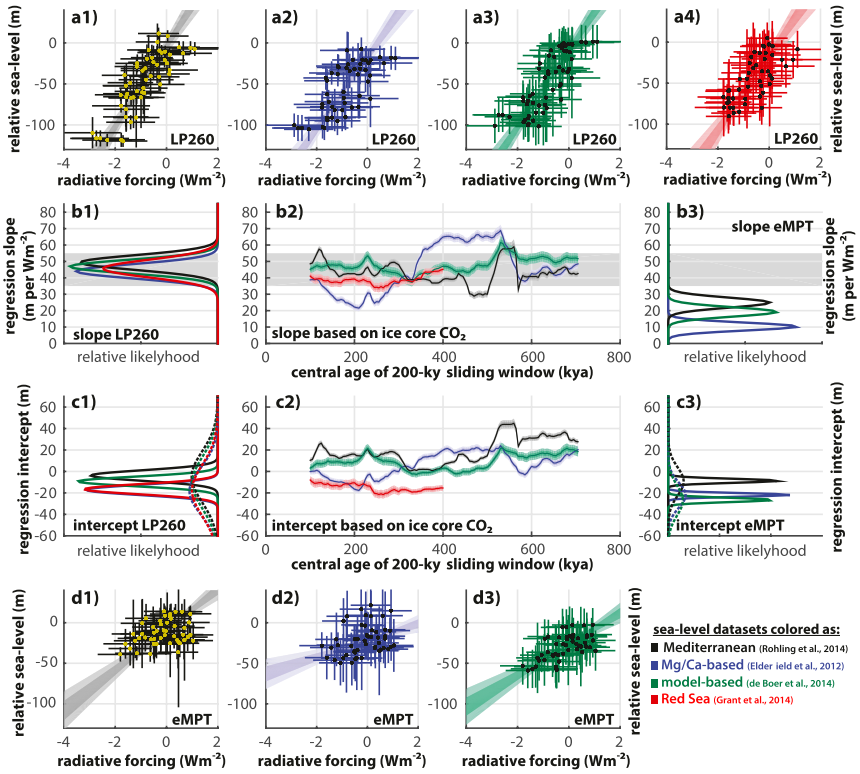

Fig. S7. Regression of relative SL change and CO_2 radiative forcing. Regression of our (*A*) LP260 and (*D*) eMPT data against different SL records (numbered 1-4 and color coded; note the Red Sea record does not extend to the eMPT period). The error bars indicate $\pm 2\sigma$ uncertainties for individual data points, and the light/dark envelope indicates the $1\sigma/2\sigma$ confidence interval of the regressions. Regression of our (*A*) LP260 and (*D*) eMPT data against different SL records (numbered 1–4 and color coded; note the Red Sea record does not extend to the eMPT period). The error bars indicate $\pm 2\sigma$ uncertainties for individual data points, and the light/dark envelope indicates the $1\sigma/2\sigma$ confidence interval of the regressions. The (*B*) slope for (*1*) LP260 and (*3*) eMPT and (*C*) intercept for (*1*) LP260 and (*3*) eMPT regressions can be compared against equivalent regression results using a (*B2* and *C2*, respectively) 200-ky sliding window of the continuous ice core CO_2 record (19), which yields relatively high slope values and intercepts around 0 m. Slopes and intercepts based on ice core CO_2 are consistent with the regression results for our LP260 data, whereas the slope regressed from our eMPT data is consistently lower. All regressions are based on the method by York et al. (61), which fully takes into account uncertainty in *x* and *y*. More discussion of methodology and uncertainty treatment is in *SI Forcing to SL Relationship*. Dashed lines in *C* indicate prediction interval.

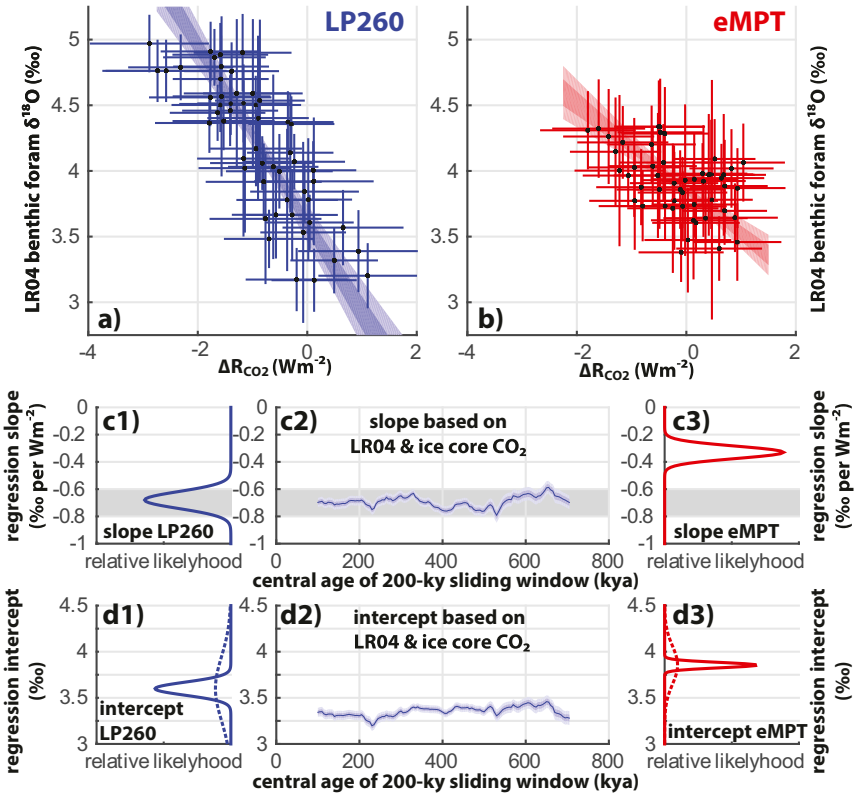

Fig. S8. Regression of $\delta^{18}O$ and $\delta^{11}B$ records. *A* and *B* display the regression results of our LP260 and eMPT boron isotope datasets against the LR04 benthic foraminifera oxygen isotope stack (Fig. S7 has details). *C* and *D* compare the results of the regression slope and intercept, respectively, with equivalent analyses using a 200-ky sliding window based on the ice core CO_2 record (*C2* and *D2*). The slopes mimic those seen in the equivalent SL analyses.

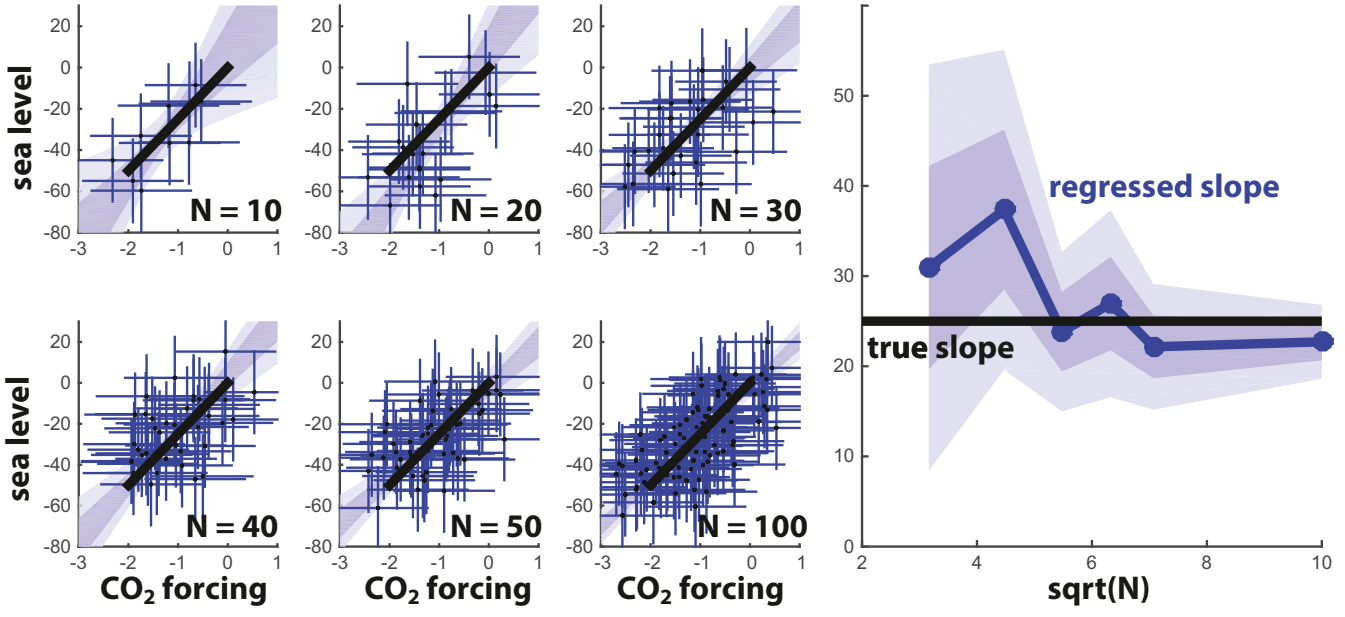

Fig. S9. Synthetic test of the York regression method. Test of regression robustness based on synthetic data that mimic our eMPT dataset. Noise is added to a known relationship of SL and CO_2 radiative forcing ($y = 25x$; shown as the fat black line) before the York regression is applied. We test the performance of the regression as a function of how many data points are contained in the dataset and find that the 51 samples in our eMPT dataset should be sufficient to recover the true CO_2 forcing to SL relationship with the required accuracy.

Table S1. Auxiliary tabulated results from the quantification of atmospheric CO_2 change since the MPT

CO_2 record(s)	Source	Percentile cutoff, %									
		5	10	15	20	25	30	35	40	45	50
Interglacial eMPT	This study, ODP 999 boron isotopes	308.23 (±17.13)	290.30 (±14.20)	286.43 (±9.61)	282.62 (±8.34)	**284.39 (±8.28)**	285.09 (±7.89)	285.61 (±7.53)	282.06 (±7.55)	285.06 (±7.01)	283.83 (±6.65)
Interglacial LP260	This study, ODP 999 boron isotopes	289.89 (±23.14)	286.55 (±13.21)	282.94 (±10.64)	277.87 (±9.67)	**277.30 (±8.82)**	276.57 (±7.40)	274.34 (±6.65)	271.29 (±6.41)	269.64 (±6.01)	268.05 (±5.51)
Interglacial eMPT-LP260	This study, ODP 999 boron isotopes	18.34 (±28.79)	3.75 (±19.40)	3.48 (±14.34)	4.76 (±12.77)	**7.09 (±12.09)**	8.52 (±10.82)	11.26 (±10.04)	10.77 (±9.90)	15.42 (±9.23)	15.78 (±8.64)
Glacial eMPT	This study, ODP 999 boron isotopes	256.04 (±22.94)	243.73 (±16.54)	237.84 (±12.26)	240.26 (±10.03)	**241.44 (±10.26)**	246.36 (±10.50)	247.55 (±10.45)	248.67 (±10.05)	253.71 (±9.93)	257.37 (±8.79)
Glacial LP260	This study, ODP 999 boron isotopes	196.33 (±19.20)	201.66 (±10.65)	201.31 (±8.50)	196.60 (±8.03)	**202.70 (±7.17)**	204.32 (±6.60)	206.91 (±6.05)	208.27 (±5.72)	210.18 (±5.64)	212.85 (±5.42)
Glacial eMPT-LP260	This study, ODP 999 boron isotopes	59.71 (±29.91)	42.07 (±19.67)	36.53 (±14.92)	43.66 (±12.85)	**38.74 (±12.51)**	42.04 (±12.40)	40.64 (±12.07)	40.40 (±11.57)	43.54 (±11.41)	44.52 (±10.33)
IG-G difference eMPT	This study, ODP 999 boron isotopes	52.19 (±28.63)	46.57 (±21.80)	48.58 (±15.58)	42.36 (±13.05)	**42.95 (±13.18)**	38.73 (±13.13)	38.06 (±12.88)	33.39 (±12.57)	31.35 (±12.15)	26.46 (±11.02)
IG-G difference LP260	This study, ODP 999 boron isotopes	93.56 (±30.07)	84.89 (±16.97)	81.63 (±13.62)	81.27 (±12.57)	**74.60 (±11.36)**	72.25 (±9.91)	67.43 (±8.99)	63.02 (±8.59)	59.46 (±8.24)	55.20 (±7.73)
IG-G difference eMPT-LP260	This study, ODP 999 boron isotopes	−41.37 (±41.52)	−38.32 (±27.62)	−33.05 (±20.69)	−38.91 (±18.11)	**−31.65 (±17.40)**	−33.52 (±16.45)	−29.37 (±15.71)	−29.63 (±15.23)	−28.12 (±14.68)	−28.73 (±13.46)
Interglacial >950 ky	Hönisch et al. (11), ODP 668B boron isotopes	311.60 (±23.88)	313.66 (±15.51)	306.50 (±14.06)	293.45 (±13.19)	**297.05 (±12.12)**	295.81 (±10.05)	291.44 (±11.35)	287.21 (±11.48)	288.19 (±9.75)	287.67 (±9.07)
Interglacial <400 ky	Hönisch et al. (11), ODP 668B boron isotopes	319.80 (±24.16)	325.45 (±18.13)	325.45 (±18.13)	321.72 (±14.76)	**312.80 (±15.07)**	307.31 (±13.52)	307.31 (±13.52)	294.65 (±12.91)	294.65 (±12.91)	288.35 (±13.05)
Interglacial >950 to <400 ky	Hönisch et al. (11), ODP 668B boron isotopes	−8.20 (±33.97)	−11.79 (±23.85)	−18.95 (±22.94)	−28.27 (±19.79)	**−15.74 (±19.33)**	−11.49 (±16.85)	−15.86 (±17.65)	−7.43 (±17.28)	−6.45 (±16.18)	−0.68 (±15.89)
Glacial >950 ky	Hönisch et al. (11), ODP 668B boron isotopes	206.01 (±15.02)	206.86 (±9.38)	211.24 (±9.11)	210.90 (±8.61)	**213.46 (±8.01)**	217.19 (±8.41)	222.01 (±8.40)	221.48 (±7.67)	219.91 (±7.12)	222.44 (±7.65)
Glacial <400 ky	Hönisch et al. (11), ODP 668B boron isotopes	176.81 (±12.88)	185.79 (±11.94)	185.79 (±11.94)	183.44 (±9.19)	**189.53 (±10.18)**	195.39 (±10.35)	195.39 (±10.35)	201.31 (±10.43)	207.41 (±11.48)	213.00 (±11.72)
Glacial >950 to <400 ky	Hönisch et al. (11), ODP 668B boron isotopes	29.20 (±19.79)	21.07 (±15.19)	25.45 (±15.02)	27.46 (±12.59)	**23.93 (±12.95)**	21.79 (±13.34)	26.61 (±13.33)	20.17 (±12.95)	12.50 (±13.51)	9.44 (±13.99)
IG-G difference >950 ky	Hönisch et al. (11), ODP 668B boron isotopes	105.59 (±28.21)	106.80 (±18.12)	95.27 (±16.75)	82.54 (±15.75)	**83.60 (±14.52)**	78.63 (±13.11)	69.44 (±14.12)	65.73 (±13.81)	68.28 (±12.07)	65.23 (±11.87)
IG-G difference <400 ky	Hönisch et al. (11), ODP 668B boron isotopes	142.99 (±27.38)	139.66 (±21.71)	139.66 (±21.71)	138.28 (±17.39)	**123.27 (±18.18)**	111.91 (±17.03)	111.91 (±17.03)	93.34 (±16.60)	87.24 (±17.28)	75.35 (±17.54)
IG-G difference >950 to <400 ky	Hönisch et al. (11), ODP 668B boron isotopes	−37.40 (±39.31)	−32.86 (±28.28)	−44.40 (±27.42)	−55.74 (±23.46)	**−39.67 (±23.27)**	−33.29 (±21.49)	−42.47 (±22.12)	−27.61 (±21.59)	−18.96 (±21.08)	−10.12 (±21.17)
Interglacial ~1,000 ky	Diverse Antarctic ice cores	277.36 (±9.98)	275.87 (±7.04)	274.42 (±5.81)	273.18 (±5.18)	**271.40 (±4.85)**	271.40 (±4.85)	269.06 (±4.98)	266.53 (±5.40)	264.06 (±5.54)	261.66 (±5.46)
Interglacial <400 ky	Diverse Antarctic ice cores	280.89 (±1.83)	277.83 (±1.29)	275.11 (±1.10)	272.56 (±1.00)	**270.26 (±0.94)**	268.21 (±0.90)	265.70 (±0.91)	263.29 (±0.95)	260.75 (±0.97)	258.31 (±0.99)
Interglacial ~1,000 to <400 ky	Diverse Antarctic ice cores	−3.53 (±10.14)	−1.96 (±7.15)	−0.69 (±5.91)	0.62 (±5.28)	**1.14 (±4.94)**	3.19 (±4.94)	3.36 (±5.06)	3.25 (±5.48)	3.31 (±5.63)	3.34 (±5.55)
Glacial ~1,000 ky	Diverse Antarctic ice cores	221.12 (±9.88)	221.39 (±7.01)	223.45 (±5.98)	225.14 (±5.25)	**226.24 (±4.77)**	226.24 (±4.77)	227.91 (±4.58)	229.66 (±4.53)	231.14 (±4.36)	232.39 (±4.13)
Glacial <400 ky	Diverse Antarctic ice cores	187.62 (±1.71)	190.61 (±1.26)	193.50 (±1.10)	195.89 (±0.98)	**197.80 (±0.90)**	199.71 (±0.87)	201.78 (±0.85)	203.91 (±0.86)	206.12 (±0.89)	208.34 (±0.92)
Glacial ~1,000 to <400 ky	Diverse Antarctic ice cores	33.50 (±10.02)	30.78 (±7.13)	29.96 (±6.08)	29.25 (±5.34)	**28.45 (±4.85)**	26.53 (±4.85)	26.14 (±4.66)	25.75 (±4.61)	25.02 (±4.45)	24.05 (±4.24)
IG-G difference ~1,000 ky	Diverse Antarctic ice cores	56.24 (±14.04)	54.48 (±9.93)	50.97 (±8.33)	48.04 (±7.38)	**45.16 (±6.80)**	45.16 (±6.80)	41.15 (±6.77)	36.88 (±7.05)	32.92 (±7.05)	29.27 (±6.85)
IG-G difference <400 ky	Diverse Antarctic ice cores	93.27 (±2.50)	87.22 (±1.81)	81.61 (±1.55)	76.67 (±1.40)	**72.47 (±1.30)**	68.50 (±1.25)	63.93 (±1.24)	59.38 (±1.28)	54.64 (±1.32)	49.98 (±1.36)
IG-G difference ~1,000 to <400 ky	Diverse Antarctic ice cores	−37.03 (±14.26)	−32.74 (±10.10)	−30.64 (±8.48)	−28.64 (±7.51)	**−27.31 (±6.93)**	−23.34 (±6.92)	−22.77 (±6.88)	−22.50 (±7.16)	−21.72 (±7.17)	−20.71 (±6.98)
Interglacial eMPT	This study, CYCLOPS model inversion	271.12 (±2.57)	267.09 (±1.87)	264.57 (±1.57)	262.57 (±1.37)	**260.82 (±1.25)**	259.24 (±1.15)	257.71 (±1.09)	256.12 (±1.05)	254.48 (±1.02)	252.83 (±1.01)
Interglacial <400 ky	This study, CYCLOPS model inversion	274.67 (±1.98)	270.09 (±1.47)	266.79 (±1.23)	263.96 (±1.10)	**261.55 (±1.02)**	259.45 (±0.94)	257.60 (±0.90)	255.74 (±0.86)	253.73 (±0.85)	251.64 (±0.85)
Interglacial eMPT to <400 ky	This study, CYCLOPS model inversion	−3.55 (±3.24)	−3.00 (±2.38)	−2.23 (±2.00)	−1.39 (±1.76)	**−0.73 (±1.61)**	−0.21 (±1.49)	0.11 (±1.41)	0.38 (±1.36)	0.75 (±1.33)	1.19 (±1.32)
Glacial eMPT	This study, CYCLOPS model inversion	207.32 (±2.50)	209.80 (±1.83)	211.89 (±1.50)	213.80 (±1.34)	**215.76 (±1.24)**	217.51 (±1.16)	219.08 (±1.09)	220.56 (±1.04)	221.91 (±1.00)	223.34 (±0.98)
Glacial <400 ky	This study, CYCLOPS model inversion	182.50 (±1.94)	186.40 (±1.43)	189.36 (±1.21)	191.80 (±1.07)	**194.03 (±0.98)**	196.19 (±0.93)	198.21 (±0.90)	200.39 (±0.88)	202.64 (±0.89)	204.99 (±0.91)
Glacial eMPT to <400 ky	This study, CYCLOPS model inversion	24.82 (±3.17)	23.40 (±2.32)	22.53 (±1.93)	22.00 (±1.71)	**21.73 (±1.58)**	21.33 (±1.48)	20.88 (±1.41)	20.16 (±1.36)	19.26 (±1.34)	18.34 (±1.34)
IG-G difference eMPT	This study, CYCLOPS model inversion	63.79 (±3.58)	57.29 (±2.62)	52.68 (±2.17)	48.77 (±1.91)	**45.06 (±1.76)**	41.73 (±1.64)	38.63 (±1.54)	35.56 (±1.48)	32.57 (±1.43)	29.49 (±1.41)
IG-G difference <400 ky	This study, CYCLOPS model inversion	92.17 (±2.78)	83.69 (±2.06)	77.43 (±1.73)	72.16 (±1.53)	**67.51 (±1.42)**	63.27 (±1.32)	59.39 (±1.27)	55.35 (±1.23)	51.08 (±1.23)	46.65 (±1.25)
IG-G difference eMPT to <400 ky	This study, CYCLOPS model inversion	−28.37 (±4.53)	−26.40 (±3.33)	−24.76 (±2.77)	−23.39 (±2.45)	**−22.45 (±2.26)**	−21.54 (±2.10)	−20.76 (±2.00)	−19.78 (±1.92)	−18.51 (±1.89)	−17.16 (±1.88)

Results are as shown in Fig. 4 and Fig. S4, with methodology as described in *SI Quantification of $^{IG}CO_2$, $^{IG}CO_2$, and $^{IG\text{-}G}\Delta CO_2$*. IG-G, interglacial–glacial. Bold values represent the middle 25% cutoff used in the paper.